Title
Optomagnetic Micromirror Platforms for Biomimetic Material Elasticity Mapping

Author
Lan, Hsin

Publication Date
2023

Peer reviewed|Thesis/dissertation

UNIVERSITY OF CALIFORNIA

Los Angeles

Optomagnetic Micromirror Platforms for Biomimetic Material Elasticity Mapping

A dissertation submitted in partial satisfaction of the requirements for the degree Doctor of Philosophy in Mechanical Engineering

by

Hsin Lan

2023

ABSTRACT OF THE DISSERTATION

Optomagnetic Micromirror Platforms

for Biomimetic Material Elasticity Mapping

by

Hsin Lan

Doctor of Philosophy in Mechanical Engineering

University of California, Los Angeles, 2023

Professor Pei-Yu Chiou, Chair

The field of mechanobiology seeks to study the interplay between cellular biophysical properties and cellular health. Of particular interest to scientists is cellular stiffness, which has been shown to play a critical role in determining cellular state. For instance, researchers have discovered that cancer cells are less stiff than their benign counterparts, and they believe that this lower stiffness enables cancerous cells to invade benign tissues and adapt to new environments. As a result, profiling cellular biomechanical state can aid in disease diagnosis, making it a crucial research area in the biomedical field.

Several methods have been proposed for measuring cellular stiffness, but most of them have limitations in terms of measuring a small number of cells or having low throughput. While

isolated single cell mechanical property sensing can provide informative clues for detecting changes in cellular states or diseases, most disease developments involve collective cell migration and tissue reorganization. Therefore, measuring collective cellular stiffness or even at the tissue-level is crucial for gaining a more comprehensive understanding of the process.

Here, my PhD research project aims to develop a device that we name "Optomagnetic Micromirror Arrays" (OMA) for steady state and real-time stiffness mapping for biomimetic materials with similar stiffness range to real biological tissues on a 5.1 mm × 7.2 mm field of view and with cellular resolution. This innovative device enables us to extract a large area of biomimetic material stiffness with single cellular resolution from the color spectra of an array of magnetic micromirrors, which are fabricated with sub-micron grating structures embedded in an elastic PDMS substrate. By applying a magnetic field at a specific orientation, the magnetic micromirrors align themselves with the field due to magnetic shape anisotropy. The color spectra of these micromirrors undergo changes, which allows us to detect the tilting angle changes of these micromirrors. This information enables us to deduce the local stiffness of the biomimetic material located on top of the micromirror array. By harnessing the power of OMA, we aim to contribute to the advancement of toolboxes in the mechanobiology field and drive forward our understanding of biological processes.

The dissertation of Hsin Lan is approved.

Tsu-Chin Tsao

Chang-Jin Kim

Arjun Deb

Pei-Yu Chiou, Committee Chair

University of California, Los Angeles

2023

TABLE OF CONTENT

LIST OF FIGURES

LIST OF TABLES

ACKNOWLEDGEMENTS

First, I would like to thank my advisor Professor Eric Pei-Yu Chiou for his guidance and support in my study and research during the past five years. His passion for technical innovation has motivated me to embrace challenges and open myself up to new opportunities. I thank Professor Arjun Deb, Professor Tsu-Chin Tsao, and Professor Chang-Jin Kim for serving on my dissertation committee and providing professional suggestions on my work.

I also appreciate my collaborators Professor Michael Alan Teitell, Dr. Berney Peng and Dr. Thang Nguyen for countless discussion with invaluable insight and knowledge in the fields of biological studies and providing indispensable cancer cells and culturing assistance for my project. I am also grateful to my collaborators Professor Amy Catherine Rowat and Minh-Tam Tran Le for the tremendous help of Nanoindentation measurement of my PDMS samples. Additionally, I thank Professor Greg Carmen, Dr. Ruoda Zheng and Emily Burnside for their help on magnetometer probe measurement and magnetics simulation work.

I would also like to thank all my colleagues from the Optofluidics Systems Lab. I thank Dr. Xing Haw Marvin Tan for being my research mentor on microfabrication techniques, simulation training, and optical setup throughout the first three years of my PhD career. His tremendous contribution to my project and my research capabilities plays an indispensable role in my career. Dr. Xiongfeng Zhu, Dr. Tianxing Man, and Dr. Pei-Shan Chung have also contributed significantly to my projects with their expertise on fabrication and optics. Many thanks go to Dr. Kuan-Wen "Dennis" Tung and Xiang Zhang for their great support and inspiration.

Finally, I would like to express my special thanks to my family for their unconditional love and my friends and pastors in church for their great mental support throughout these years.

VITA

Professional Employment

2018	Research Assistant
	Academia Sinica, Taipei, Taiwan
2016-2018	Research Associate
	Silicon Kinetics Inc., San Diego, USA

Education

2014 – 2015	M.S., Nanoengineering
	University of California, San Diego, USA
2008 – 2013	B.S., Mechanical Engineering
	National Taiwan University, Taipei, Taiwan

Publications

[1] Li, J., Yu, X., Xu, M., Liu, W., Sandraz, E., **Lan, H.,** Wang, J. and Cohen, S.M., 2017. Metal–organic frameworks as micromotors with tunable engines and brakes. *Journal of the American Chemical Society*, *139*(2), pp.611-614.

Chapter 1. Introduction

1.1 Introduction to cell mechanics

Cellular biomechanical properties have been the subject of increasing interest in recent years due to their potential as important clues to study the health state of cells and tissue behaviors [1]. These properties describe the mechanical response of cells to external stimuli, such as mechanical forces in the extracellular environment, or cellular deformability (effective stiffness) and provide insights into the structural and functional changes occurring within cells. The mechanical properties of cells are closely related to their internal structures and molecular composition, including cytoskeletal proteins, nucleus, membrane lipids, and cellular organelles [2]. Changes in these cellular components can affect the mechanical properties of cells, leading to alterations in their deformability or stiffness [3]. This, in turn can have a significant impact on cellular functions, such as migration [4], proliferation [5], and differentiation [6].

The mechanical properties of cells, particularly their stiffness, have emerged as essential biomarkers that provide valuable insights into cellular behaviors and functions. The cytoskeleton plays a pivotal role in these processes. For example, cells with a well-organized cytoskeleton tend to be stiffer and more resistant to deformation than cells with a disorganized cytoskeleton [7]. The cytoskeleton is composed of three major structural elements: actin filaments, intermediate filaments, and microtubules, which all contribute to the overall stiffness of cells [8-13].

The reorganization of cytoskeletal structures can be triggered by pathological mechanisms, leading to modifications in the elastic modulus of living cells [14]. The correlation between cell stiffness and the presence of pathological cells has been extensively studied [15][19]. Irregular variations in cell stiffness have been noted in various diseases, such as cancer

[16], cardiovascular disease [17], and neurological disorders [18]. Among these, cancer is of significant interest for investigation. It has been widely reported that cancerous cells exhibit lower stiffness than their benign counterparts [19], which could be attributed to the compliance facilitating the invasion process. Moreover, researchers have validated the link between malignancy and the disorganization of the cytoskeleton, as cancer cells often exhibit increasingly disorganized cytoskeletal structures [20][21].

Mutations in cytoskeletal proteins have been linked to the development of certain types of cancer, suggesting a potential role for the cytoskeleton in the pathogenesis of cancer [22]. For instance, studies have shown that invasive tumor cells tend to modify their adhesion to the extracellular matrix, which allows them to mechanically soften and escape from the primary tumor [23][24]. These changes in mechanical properties are believed to be driven by alterations in the cytoskeleton, particularly the actin cytoskeleton [25]. Consequently, these findings suggest that changes in the cytoskeleton may serve as valuable biomarkers for the early detection and diagnosis of cancer, as well as potential therapeutic targets for cancer treatment [2].

In addition, recent research has established a strong link between the cellular phenotype, particularly cellular stiffness, and the metastatic potential of cancer cells [21][26]. Metastasis is the process by which cancer cells spread from their primary location to other parts of the body. Highly metastatic cells typically express fewer adhesion receptors and exhibit increased protease activity, which helps them detach from their surroundings [31]. Numerous studies have shown that cancer cells with lower stiffness are more likely to metastasize than those with higher stiffness [27][28].

Recent technological advancements have facilitated precision measurement and manipulation of the mechanical properties of cells in vitro, enabling researchers to gain a better

understanding of the intricate relationship between cellular biomechanics and cellular behavior. In the following sections, we will explore some key technologies that have been developed for the measurement of cellular stiffness as well as their potentials.

1.2 Current approaches for cellular stiffness measurement

Cytoskeleton, which is composed of dense intracellular biopolymeric networks, plays a critical role of cellular architecture. In many cases, change to cellular structure and mechanical property, such as elasticity or resistance to deformation, are associated with cell shape and motility. Pathogenic processes can cause the reorganization of cytoskeletal structures, leading to changes in the elastic modulus of living cells. For instance, researchers have found that cancer cells tend to have a more compliant morphology than benign cells, which may facilitate the invading process into other tissues. Therefore, investigating the relationship between cellular stiffness and disease states can provide valuable insights into the underlying mechanisms driving disease progression.

1.2.1 Atomic force microscopy (AFM)

Atomic Force Microscopy (AFM) indentation testing is a widely used technique for measuring cellular biomechanical properties. AFM utilizes a compliant cantilever beam with a sharp tip mounted at its end to measure the profile of objects of interest, such as cells or biological materials. In AFM indentation testing, a laser is shone at the cantilever beam, and the resulting reflection is detected by a photodetector. This process allows for the calculation of deflection, which can be used to determine the topography or stiffness of the object being analyzed.

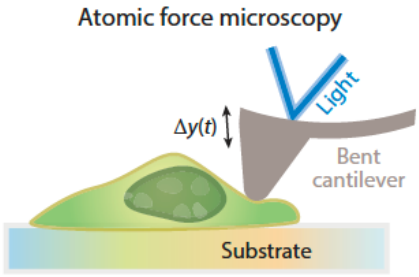

Figure 1.1. Illustration of AFM for cellular stiffness measurement [2].

The advantage of using AFM indentation testing lies in its ability to provide high-resolution imaging and mapping of cellular biomechanical properties, such as stiffness, at the sub-cellular level. Moreover, it enables the investigation of various factors, such as drugs or environmental stressors, on cellular stiffness, leading to the discovery of novel mechanobiological mechanisms underlying various diseases [31][32]. AFM indentation testing also offers several advantages over other techniques, such as its adjustability in selecting different probe shapes and beam spring constants [33]. These features allow for the measurement of different types of cells and their stiffness properties, making AFM-based tests a versatile and powerful tool in cellular biomechanical research.

In AFM, spherical probes are typically used to measure cellular stiffness in liquid environments. This approach enables the application of the Hertz or Sneddon model to characterize the force as a function of the indentation depth [34][35]. The Hertz model is commonly used for indenting soft materials, such as biological samples, and it assumes that the sample is an elastic half-space. This model calculates the sample's Young's modulus, a measure of its stiffness, from the force and indentation depth. On the other hand, the Sneddon model is used to characterize the indentation of a sample with a flat punch, such as the AFM cantilever

tip, into an elastic material. This model assumes that the sample is an elastic half-space with a power-law relation between the force and indentation depth.

The use of atomic force microscopy (AFM) to study cellular stiffness has yielded promising results in the field of cancer research. In a review article by Lekka [36], the stiffness of various cancer cells was compared to that of their healthy counterparts using AFM. The studies showed that the Young's modulus ratio of healthy cells to cancer cells ranges from 2 to 32, indicating significant differences between the two and suggesting that cellular stiffness may serve as a determinant for cancer detection and diagnosis.

In the context of cancer cell metastasis, researchers have utilized AFM to probe the stiffness of cancer cells with varying grades and have observed a correlation between the Young's modulus of the cells and their metastatic potential. For example, Liu et al. [37] investigated the stiffness of bladder cancer cells with different grades (RT4 and T24) and found that the higher-grade cancer cell line (T24), which possesses higher metastatic potential, exhibited lower Young's modulus than the other (RT4). Similarly, Xu et al. [38] studied the stiffness of ovarian cancer cells and found that highly invasive ovarian cancer cells (HEY A8) show lower Young's modulus relative to their less invasive parental cells (HEY). These studies demonstrate the potential of AFM as a functional tool in evaluating the metastatic potential of cancer cells.

Aside from cancer cells, Dulinska et al. carried out erythrocyte's (red blood cells) stiffness measurements using AFM [39]. In their study, the mapping by AFM of normal erythrocytes and erythrocytes with G6PD deficiency, which is a hereditary disease characterized by causing hemolytic anemias, have shown that erythrocytes with G6PD deficiency have 3 times larger Young's modulus than normal cells and exhibit a flatten shape. This result suggests AFM

can be employed not only to characterize cellular structural alterations typical for certain blood diseases but also to monitor pathological states.

1.2.2 Micropipette Aspiration

Micropipette aspiration (MA) is another widely used method to measure cellular elastic or viscoelastic properties by applying a suction pressure (P) to a cell and measuring the resulting cellular deformation (ΔL). MA has the advantage over AFM in that it can achieve both local and whole-cell measurements [40]. Additionally, MA can also be integrated with microfluidic systems to reach high-throughput sensing. This approach has been originally applied to red blood cells at the early age in its development [41] and extended to various cell types such as cancer cells [42].

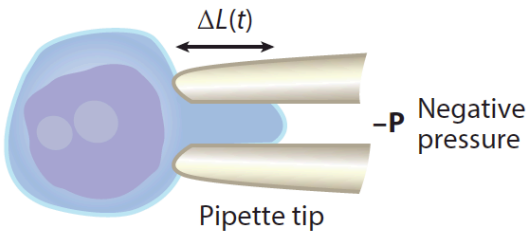

Figure 1.2. Illustration of micropipette aspiration for cellular stiffness measurement [2].

Different cellular components require different pressure thresholds for measurement. For example, a pressure of 1 Pa is required for measuring cell membrane suction, while 500 Pa is needed for measuring the cytoskeleton and nucleus [43]. Rowat et al. also established a model for diseased mouse embryo fibroblasts whose nucleus volume changes while being aspirated into the micropipette. This model is distinct from that of red blood cells or vesicles whose volume

remain unchanged due to osmotic stabilization and can be utilized for the cells whose nucleus volume changes during aspiration.

Shojaei-Baghini et al. have conducted a study to differentiate between benign and malignant urothelial cells based on their stiffness using MA [42]. Their results indicate that malignant urothelial cells exhibit lower Young's modulus compared to benign cells. Interestingly, the malignant cells with a higher nucleus-cytoplasmic ratio (NC) demonstrated a higher Young's modulus than the malignant cells with a lower NC. This finding suggests that the relationship between cellular stiffness and malignancy is influenced by the nucleus-cytoplasmic ratio, which reflects changes in the cellular phenotype. By utilizing MA, this study provides a unique perspective in understanding the mechanical properties of cancer cells and highlights the potential of this technique for cancer diagnosis and treatment.

1.2.3 Optical Tweezer

Optical tweezers are a non-contact manipulation technique that uses a highly focused laser beam to trap and move microscopic particles. When a microparticle encounters a laser beam, the beam exerts two forces on the particle: the gradient force and the scattering force. The gradient force is the dominant force that traps and moves particles. It arises when the electric field of the laser beam induces a dipole moment in a dielectric particle with a size smaller than the wavelength of light (Rayleigh scattering region), resulting in a gradient force towards the region of highest intensity. The gradient force drives the particle to where the dipole energy is minimum, which is the location where the laser beam intensity is highest. The scattering force is caused by the transfer of momentum from the photon to the particle as it scatters, which points toward the direction of light propagation [44]. The interplay between the gradient force and the

scattering force can lead to the trapping of particles in a certain position. A small particle experiences a gradient force that pulls it towards the focal point and a scattering force that pushes it away from the direction of incidence. These forces balance each other, resulting in a stable trapping position for the particle.

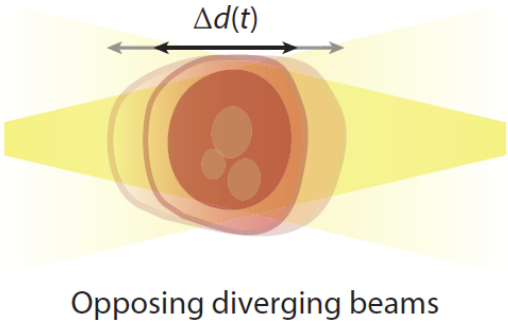

Figure 1.3. Illustration of optical tweezer for cellular stiffness measurement [2].
The gradient force and the scattering force from a focused laser beam balance each other to trap a nanoparticle.

When particles are larger than the wavelength of light, they act as refractive objects. The gradient force for this case arises from the unequal optical momentum on the particle when it is not in its equilibrium position, and it pulls the particle towards the focus. The reflection force, same as the previous case, comes from scattering and pushes the particle in the direction of light propagation. These two forces balance each other out, resulting in a stable trapping position for the particle [45].

In optical tweezers, a high numerical aperture (NA) lens is essential to create a large gradient force and achieve accurate calibration of the trapping force. Prior to using optical trapping, it is important to calibrate the trapping force using one of several methods. One common approach is to analyze the power spectrum of Brownian motion of a trapped particle to obtain the trapping stiffness [46]. Another approach is to apply an external force on the particle

while it is held in the optical trap. Since the optical trapping force tends to restore the particle position, it can be calibrated by adjusting the external force when they reach equilibrium [45].

When measuring cell stiffness with optical tweezers, researchers typically apply the optical tweezers to beads attached to the cells for mechanical deformation. The force applied by optical tweezers is in the piconewton range, which is only sufficient for moving a bead. By measuring the displacement of the bead and a calibrated force with accurate position detection systems, researchers can extract cellular stiffness and monitor changes over time [47]. Suresh et al. used optical tweezers to monitor progressive changes in the mechanical properties of human red blood cells (RBC) infected with the malaria parasite *Plasmodium falciparum*. They found that the shear modulus of RBCs infected with malaria can increase up to 10-fold during parasite development, which is much higher than previously thought [48].

Alternatively, Guck et al. measured cellular stiffness of human breast epithelial cells and monitored the progression from normal to metastatic state using optical tweezers with two laser beams integrated with microfluidic systems [49]. The two laser beams can generate sufficient force (nanonewton range) to directly stretch the cells without the need for beads. The results show that the elasticity of human breast epithelial cells changes from high to low with the progression of metastasis, suggesting cellular deformability as an inherent biomarker for biological development investigation and disease diagnosis.

While optical tweezers offer several advantages such as high accuracy and non-contact measurement, they are not without their limitations. One of the main disadvantages of using optical tweezers is their low throughput, as they are typically used to measure the mechanical properties of individual cells one at a time. However, recent advances in microfluidic systems have made it possible to integrate optical tweezers with microfluidic devices [50], allowing for

the parallel measurement of multiple cells at the same time, thus significantly increasing the throughput of the technique. Optical tweezers with two laser beams also have potential to apply larger force for broader applications by increasing the laser power, but extra care needs to be taken for local heating concern [51].

1.2.4 Magnetic Tweezers

The investigation of cellular mechanical properties, both internally and locally, has become a focal point in the field of cell mechanics. An emerging and valuable approach, magnetic tweezer, involves the utilization of magnetic beads, enabling the assessment of both elastic and viscoelastic properties of cells. This technique involves applying a linear force or a twisting torque to magnetic microbeads that are either internalized by or attached to cells, enabling the physical manipulation of cellular structures. By monitoring the motion of these microbeads using a high-resolution imaging system, cellular mechanical properties can be probed and characterized [52][53].

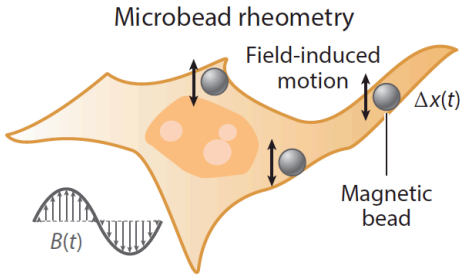

Figure 1.4. Illustration of magnetic tweezers [2].

Magnetic tweezers or magnetic bead rheometry apply magnetic microbeads attached to internalized by cells subjected to a magnetic field gradient or magnetic torque. By observing the displacement or rotation of magnetic beads, the corresponding cellular elasticity or viscoelasticity can be extracted.

In the case of applying a linear force, the device typically consists of one or more electromagnetic poles comprising a para- or ferromagnetic core wrapped with wires. These electromagnetic poles generate a magnetic field gradient that attracts the micromeads towards the poles, enabling the application of forces on cells. By tracking the displacement of the microbeads, the viscoelastic properties of cells can be extracted. To enhance the magnetic force, a sharp tip connected to the pole can be designed to converge the field. However, a single pole design may suffer from heterogeneous force distribution. To achieve uniform forces over an area, multiple tips can be arranged with different current amplitudes and directions, resulting in a nearly uniform magnetic force field. Therefore, current multipole designs enable the manipulation of multiple beads simultaneously by creating a nearly constant field gradient over an area spanning tens to hundreds of cells. The selection of magnetic materials is crucial. Ferromagnetic materials provide larger forces but retain a higher level of magnetization even after the magnetic field is removed. On the other hand, paramagnetic materials are less affected by magnetization but are also less responsive to magnetic fields, resulting in smaller forces in the piconewton to nanonewton range.

Magnetic twisting is another method for manipulating magnetic beads, where instead of linear movement, a magnetic torque is applied to twist the beads. In this approach, the magnetic beads are initially magnetized to a specific orientation using an applied magnetic field. When the magnetic field is then applied in a different direction, the beads experience a twisting torque as they realign with the new field. The resulting rotation of the beads is characterized by a tendency to decrease the torque between the induced magnetization in the beads and the applied field.

Magnetic tweezers have emerged as a valuable tool for distinguishing between cancer cells and normal cells, as well as determining the metastatic potential of cancer cells. In a study

by Swaminathan et al. [54], magnetic tweezers were employed to investigate different cancer cell lines with varying invasiveness. The results revealed a compelling finding: the most invasive cell line exhibited a 10-fold higher deformability compared to the least invasive cell line. This discovery highlights a power-law relationship between cell stiffness and the invasiveness of cancer cells.

Furthermore, the study also shed light on the impact of modulating cell stiffness on invasiveness. Pharmacological inhibition of myosin II, which reduced cell stiffness, led to an increase in invasiveness. Conversely, increasing cell stiffness through the restoration of metastasis suppressor TbRIII/betagly expression resulted in a decrease in invasiveness. These findings provide insights into the interplay between cellular stiffness and the invasiveness of cancer cells, offering potential avenues for therapeutic interventions and the development of novel strategies to mitigate cancer metastasis.

1.3 Motivation for large area cellular stiffness measurement

The aforementioned techniques offer high-resolution or relatively high-throughput measurement of cellular stiffness. However, they are limited to measuring the stiffness of single cells or a small number of cells at a time, and are not capable of measuring a large area simultaneously.

While isolated single cell mechanical property sensing can provide informative clues for detecting changes in cellular states or diseases, most disease developments involve collective cell migration and tissue reorganization. These processes demonstrate distinct behaviors from single cells and require the measurement of the biomechanical properties of collective cells in a large area to gain a comprehensive understanding of the underlying mechanisms. Therefore, it is

crucial to develop methods that enable the concurrent measurement of the biomechanical properties of a large population of cells in a given tissue or cell sheet.

1.3.1 Collective cell behaviors and characteristics

Collective cell migration refers to the coordinated movement of cells as a collective entity, exhibiting organized patterns such as sheet formation, clustering, or streaming. This phenomenon can be observed in cultured cell sheets as well as in vivo, playing a role in various biological processes including tissue regeneration, cancer metastasis, and tumor neovascularization. However, collective cell migration is not simply a result of individual cells moving together in unison. It encompasses intricate interactions and cooperative behaviors within the cell group, leading to enhanced migration efficiency and complex dynamics within the collective [55][56].

Within collective cell groups, cells engage in interactions not only with their surrounding extracellular matrix (ECM) via focal adhesions or hemidesmosomes but also with neighboring cells. These intercellular interactions encompass various types of adhesive structures. Mechanobiology studies have revealed that both cell-ECM and cell-cell adhesions play a role in mechanosensing, allowing cells to convert mechanical stimuli into biochemical signals that contribute to cell migration [58]. For instance, in a study conducted by Barriga et al. [57], they observed that the stiffening of head mesoderm tissue leads to an epithelial-to-mesenchymal transition in neural crest cells, subsequently triggering their collective migration., which indicates neural crest cells can utilize their mechanosensing capability to detect changes in their microenvironment and respond accordingly.

Through adhesion, force-dependent mechanisms, and signaling interactions, cells within a group influence and differentiate from one another, leading to the emergence of leaders and followers and promoting coordinated migration. These dynamic variations are crucial for achieving directed movement. Moreover, certain cell types have been observed to exhibit rotational migration within confined spaces, adding further complexity to collective cell migration dynamics [59].

Cell migration tendency also serves as a valuable indicator of cellular state, and dysregulated cell migration is frequently implicated in disease progression, including the invasion and metastasis of cancer. Histopathological analyses often reveal the collective invasion of squamous cell carcinomas in the form of clusters or strands, highlighting the importance of collective cell migration in disease pathogenesis [60][61]. Within collectively migrating and invading cancer cells, the presence of leader cells and follower cells is observed [59], reflecting distinct gene expression profiles between them. Leader cells play a crucial role in facilitating cancer invasion by sensing microenvironmental cues, establishing and navigating invasion tracks, and coordinating with follower cells to promote efficient invasion processes [62-64]. This ability to invade and metastasize is often correlated with the migration tendency and motility of cancer cells. For example, in patients with advanced-stage ovarian cancer, primary cells derived from ascites demonstrate varying degrees of invasiveness among different cell lines. The most invasive cell line shows significantly greater migratory potential than the least invasive cell line, highlighting the importance of cancer cell migration in the progression of the disease [65]. This study has also established a correlation between cellular stiffness and invasiveness in cancer cells through the measurement with magnetic tweezers. Their research has shown that the most invasive cancer cells exhibit ten times less stiffness than their least invasive counterparts. In

contrast, another study demonstrated that prostate cancer cells treated with anticancer drugs exhibited higher stiffness and lower invasiveness potential [66].

The observed correlations among cancer cell stiffness, metastatic potential, and invasion tendency underscore the significance of measuring the biomechanical properties of collective cells over a large area, which may provide valuable insights into the mechanisms driving cancer progression. Despite its potential, such a technology is currently unavailable, highlighting the need for further advancements in this field.

1.3.2 Tissue stiffness dictates disease states

As mentioned previously, the behavior of collective cells differs significantly from that of individual cells, and it is characterized by increased heterogeneity due to the presence of various components such as the extracellular matrix (ECM). The ECM plays multiple roles within cell groups and tissues, including facilitating normal wound healing processes. However, excessive deposition of ECM can lead to organ dysfunction. Fibrotic diseases, such as pulmonary fibrosis and cardiovascular disease, are typically characterized by the abnormal proliferation of fibroblasts, their differentiation into myofibroblasts, and the excessive synthesis and secretion of ECM components [67].

Similarly, significant alterations in extracellular matrix (ECM) remodeling, resembling those seen in fibrotic diseases, play a pivotal role in tumor progression. In the context of breast cancer, the tissue undergoes pronounced changes, with stiffness reaching up to 10 times higher levels than in normal breast tissue (1.5 kPa and 150 Pa, respectively) [68][69]. Notably, a region of stiffer tissue is often observed at the tumor margin of invasive tumors. Furthermore, increased matrix stiffness and ECM remodeling have been identified in pre-malignant tissue, suggesting

their involvement in the process of malignant transformation within the breast. In contrast, a reduction in cellular tension can repress the malignant phenotype of mammary epithelial cells and subsequently eliminate the malignant behavior of cancer cells [70]. These findings emphasize the significant role of extracellular matrix (ECM) dynamics in influencing tumor behavior, underscoring the importance of comprehending the mechanical properties of the tumor microenvironment in cancer research. However, the precise mechanisms underlying tumor progression and metastasis are still not fully understood [71].

The observation of softer individual cancer cells in comparison to their normal counterparts may appear contradictory to the common perception of cancer tissues being stiffer than normal tissues. The increased stiffening of primary tumors detected by macroscopic measurements revealed that the extracellular matrix components seem to play a crucial role in providing mechanical properties of tissues and subsequently, the malignant progression of cancer [72]. Therefore, while individual cancer cells may exhibit softer characteristics compared to their normal counterparts, the overall stiffness of cancer tissues is influenced by the changes in the ECM. These complex interactions between cancer cells and the ECM highlight the complex nature of cancer tissues and the diverse mechanical properties present within the tumor microenvironment [73].

Indeed, when measuring tissue stiffness using AFM, it has been observed that there are wide distributions of the Young's modulus [74-76]. This variability in stiffness can be attributed to the heterogeneous nature of tissue samples. Specifically, within these heterogeneous tissue samples, smaller Young's modulus values can be attributed to the elasticity of individual cells. Cells exhibit a certain level of flexibility and deformability, which contributes to the overall tissue compliance. On the other hand, larger Young's modulus values are often associated with

the presence of extracellular matrix components, such as collagen fibers, which form dense deposits in several types of cancer [70][74].

Various techniques are available for measuring tissue stiffness, and they can be broadly categorized into those that assess tissue samples as bulk materials, such as tensile testing [77][78], compression testing [78], and shear rheometry [79], and those that probe local stiffness, such as AFM [80] and micropipette techniques [81].

Macroscopic measurements provide valuable information about the bulk properties of tissues. However, it is important to acknowledge that there can be differences between macroscopic and microscopic material properties [83]. At the nanoscale or microscale dimensions, the moduli of materials may not only vary but also exhibit size dependence, challenging the traditional macroscopic definition of Young's modulus as an intrinsic material property. Additionally, tissues are highly heterogeneous, and relying solely on bulk material properties may not fully capture their true characteristics.

Conversely, techniques that probe local stiffness offer insights into specific areas but are limited in their ability to provide a comprehensive understanding of tissue-level stiffness distribution. These methods typically focus on small regions of the tissue, which may not represent the entire tissue's mechanical behavior.

1.3.3 The missing link between single cells and tissue stiffness

In order to quantify the mechanical properties of a population of interacting cells, as seen in collective cell migration and tissue regeneration, it is crucial to employ an experimental approach that integrates multivariate single-cell techniques and enables traceability of spatial dynamics. This technique should effectively bridge the spatial scales ranging from subcellular

resolution (micrometer range of cells) to tissue organization (ranging from millimeters to centimeters), allowing for comprehensive measurements at both scales [82]. By establishing such an approach, we can gain a deeper understanding of how the collective properties of cells emerge from their individual behaviors and contribute to complex biological processes.

As previously discussed, existing tools for subcellular stiffness measurement have provided valuable insights into cellular structure and properties. However, these techniques often suffer from limitations such as low throughput or small detection areas, limiting their applicability. On the other hand, current techniques for tissue-level measurements predominantly focus on the bulk properties of biological tissues and lack the capability to simultaneously probe the local stiffness at the micron scale. Moreover, there are still challenges to overcome when it comes to measuring mechanical properties and imaging tissue samples concurrently. A major obstacle in tissue imaging is the opacity of the samples, which hinders accurate visualization and analysis.

There is a need for an experimental framework that combines high-throughput, large-scale measurements with the ability to assess both subcellular and tissue-level stiffness mapping. Such a framework would bridge the gap between subcellular resolution and tissue organization, enabling a comprehensive understanding of the interplay between cellular properties and tissue-level behavior. Overcoming the limitations in current techniques and addressing the challenge of sample opacity will also be crucial for advancing our understanding of biological systems and facilitating the development of novel diagnostic and therapeutic approaches.

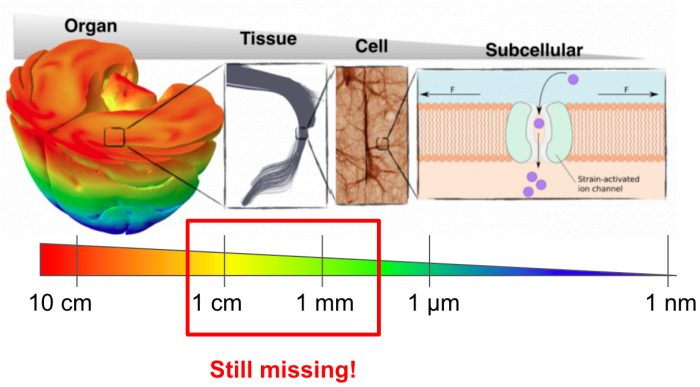

Figure 1.5. The spatial scale of biological stiffness measurement.

Current techniques for measuring biological stiffness are limited to specific spatial scales. Conventional approaches, as discussed in Section 1.2, allow for the measurement of single cells or subcellular structures. Similarly, there are established methods for measuring the stiffness of larger-scale biological tissues, as mentioned in Section 1.3.2. However, there is a lack of approaches that cater specifically to intermediate scales of stiffness measurement.

Chapter 2. Optomagnetic Micromirror Arrays

2.1 Proposed device overview

Here, we present the Optomagnetic Micromirror Arrays (OMA) as a versatile platform capable of mapping the concurrent and real-time biomimetic material elastic modulus over a large area of 5.1 mm × 7.2 mm with single cellular resolution. OMA comprises of more than 50,000 magnetic micromirrors, each having a sub-micron grating structure, that are affixed to a flexible PDMS membrane. The platform utilizes white light illumination and a color camera for image detection. By subjecting OMA to a uniform magnetic field rotation at a specific angle to the device, the magnetic micromirrors tend to align with the magnetic field direction due to magnetic shape anisotropy, resulting in changes in their tilting angles. Consequently, the tilting angle change can be quantitatively measured by collecting the color change of each micromirror using the image sensor in camera. When biomimetic materials resembling collective cells or tissues of different stiffness are seeded onto the micromirrors, they create different rotation resistances and cause micromirrors under them to display different colors. By monitoring the color changes of these micromirrors under the glass substrate, we can map the stiffness of materials on top without the concern of biological samples' opacity (Figure 2.1 and 2.2).

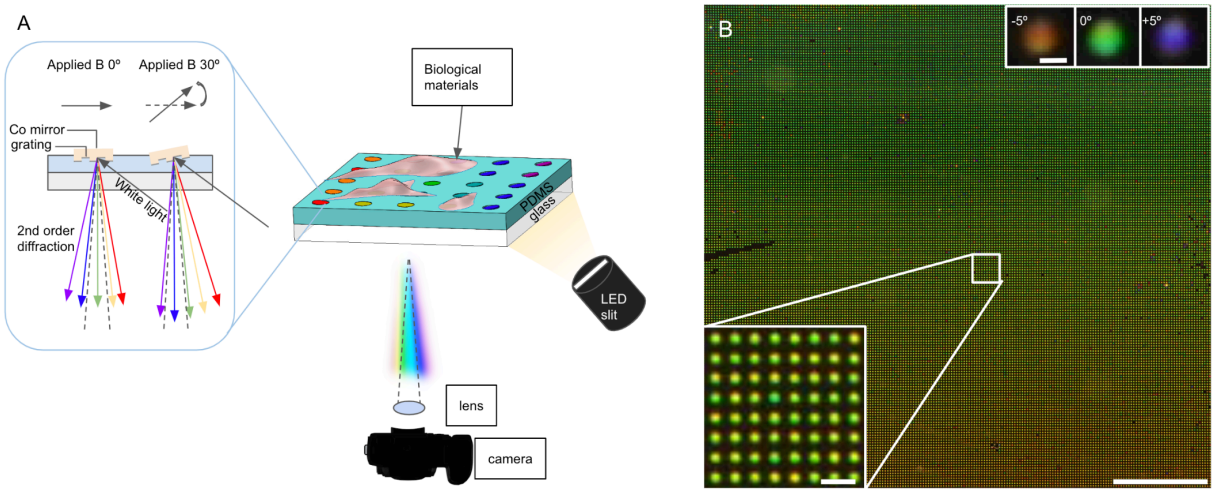

Figure 2.1. Illustration of the OMA platform

(A) Our OMA platform is composed of magnetic micromirrors with sub-micron gratings bonded periodically on top of a soft PDMS film. Diffraction grating splits the illuminated white light from LED slit into a color spectrum collected by the lens under the device, which avoids the opacity concerns from the biological materials on top. When applying a uniform magnetic field B with a certain angle out of plane, the easy axis of magnetic micromirrors will align with the magnetic field direction due to shape anisotropy and rotate the micro-mirrors. The detected color ranges are different before and after magnetic actuation due to micro-mirror tilting.

(B) Image of the OMA device showing a field of view of 5 mm × 5 mm. (inset, bottom left) Zoomed in area of the OMA device showing individual diffraction grating mirrors. (inset, top right: -5, 0 ,+5 degree) The sub-micron grating structure enables the micromirrors to diffract different colors with different tilting angles. Scale bars: (bottom right: 1mm), (inset, bottom left: 50 μm), (inset, top right: 10 μm).

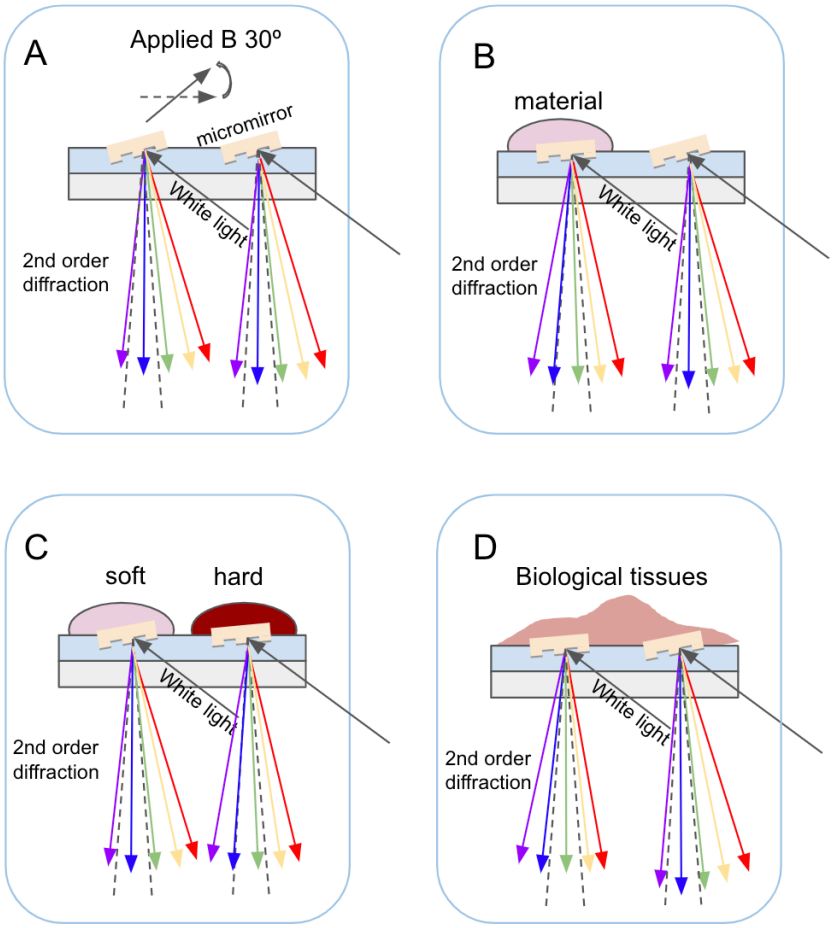

Figure 2.2. Material local elastic modulus measurement mechanism

With a uniform magnetic field B applied on the micromirrors, magnetic micromirrors will tend to align with the applied field and have an out-of-plane tilt. Different tilting angles among each micromirror caused by material stiffness difference on top can be extracted by color detected. Four different cases are illustrated as follows: (A) Without any material on top, all micromirrors have the same tilting angle. (B) With material on parts of the micromirrors, those micromirrors will have smaller tilting angles comparing to the others. (C) With soft and hard material on different locations, the micromirrors with harder material will have smaller tilt comparing to the ones with softer material. (D) Biological materials with heterogeneous stiffness on top. Each location will experience different stiffness and different tilting angles.

2.2 Optics fundamental

2.2.1 Optical interference principle

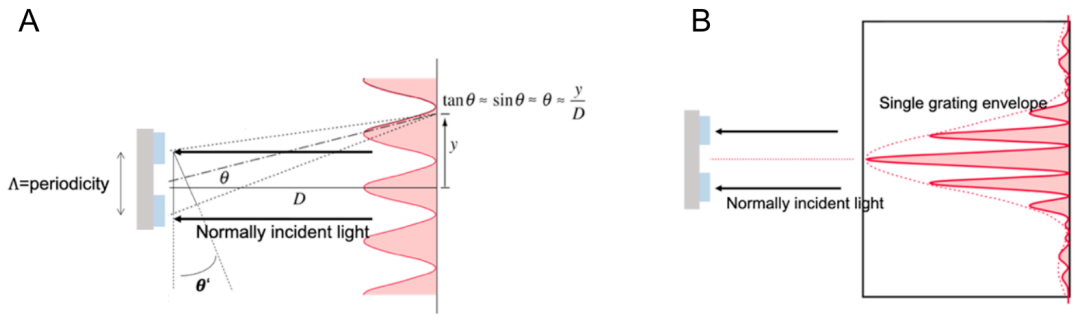

Figure 2.3. The illustration of reflective gratings.

(A) The diffraction illustration on (two) reflective gratings without considering grating width(B) The real diffraction pattern on (two) reflective gratings (modified from http://hyperphysics.phy-astr.gsu.edu/).

The main principle of OMA is based on measuring the tilting angles micromirrors with optical signals diffracted from the grating structures. The Huygens-Fresnel principle describes the optical diffraction phenomenon, which treats each point in a propagating wavefront as a collection of individual spherical wavelets. When light interacts with a grating structure that has a comparable linewidth to the optical wavelength, it bends and creates a characteristic diffraction pattern. This is caused by the interference of different points on the wavefront that travel different path lengths to the registering surface. Figure 2.3A depicts the case of two reflective gratings, similar to the well-known Young's double-slit interference pattern. When $D >> \Lambda, \theta' \approx \theta$ and the optical path difference from the two grooves can be expressed as $\Lambda sin\theta$, where Λ is the periodicity of the gratings. Therefore, when

$$\Lambda sin\theta = m\lambda \qquad \text{(eqn. 2.1)}$$

where m is an integer, there will be a constructive interference on the screen, namely, the bright spots. On the other hand, when

$$\Lambda sin\theta = \left(\mathrm{n} - \frac{1}{2}\right)\lambda \qquad \text{(eqn. 2.2)}$$

where n is an integer, there will be a destructive interference, which forms the dark spots. The position of each bright spot can be calculated by:

$$m\lambda = \Lambda sin\theta \approx \Lambda tan\theta = \frac{y}{D} \qquad \text{(eqn. 2.3)}$$

where y is the position on the projected plane.

2.2.2 Optical diffraction principle

According to Fraunhofer diffraction theory, when the distance between the aperture and the screen (D) is significantly larger than the aperture diameter (d), (D/d >> 64000), the resulting diffraction pattern will represent the directed Fourier transform of the aperture distribution. In the case of our device, the aperture corresponds to the grating structure embedded within it:

$$U(x,y) = \frac{e^{jkz}e^{j\frac{k}{2z}(x^2+y^2)}}{j\lambda z}\iint_{-\infty}^{\infty} U(\xi,\eta)\exp\left[-j\frac{2\pi}{\lambda z}(x\xi + y\eta)\right]d\xi d\eta \qquad \text{(eqn. 2.4)}$$

where U is the field distribution; x and y are the coordinates on the screen; ξ and η are the coordinates on the aperture (grating in our case). By considering these coordinates, the intensity profile on the screen is essentially a Fourier transform of the light that is illuminated and reflected from the grating structure.

Therefore, the diffraction phenomenon at the grating width plays a crucial role in shaping the intensity profile on the screen. Similar to the concept of single-slit diffraction, the interference pattern is confined within this diffraction envelope. Figure 2.3B illustrates this phenomenon. To obtain the light profile in terms of intensity versus position, we multiply the

expression for double-grating interference by the expression for single grating diffraction. This assumption is made under the premise that the multiple-grating arrangement consists of identical gratings. Additionally, we can extend this expression to cover scenarios involving multiple gratings. Figure 2.4 showcases the interference pattern resulting from five gratings. Based on Fraunhofer diffraction theory, the light intensity profile can be mathematically expressed as follows:

$$I(\theta) = I_0 \left(\frac{\sin\beta}{\beta}\right)^2 \left(\frac{\sin N\alpha}{\sin\alpha}\right)^2 \qquad \text{(eqn. 2.5)}$$

where $\beta = \frac{ka\sin\theta}{2}$, $\alpha = \frac{k\Lambda\sin\theta}{2}$, k is wave vector, a is grating width, Λ is the grating periodicity, N is the grating number. From the equation, the position of each bright spot can be calculated as:

$$\Lambda\sin\theta = m\lambda = \frac{2m\pi}{k} \Longrightarrow \alpha = \frac{k\Lambda\sin\theta}{2} = \frac{k\Lambda}{2}\frac{y}{\sqrt{D^2+y^2}} = m\pi \qquad \text{(eqn. 2.6)}$$

Therefore, it is important to note that the number of grating grooves does not affect the position y on the screen. However, it does influence the width of each bright spot, as depicted in Figure 2.4. The profile of the interference pattern remains consistent in terms of its position along the y-axis, while the number of grooves determines the width of the bright spots.

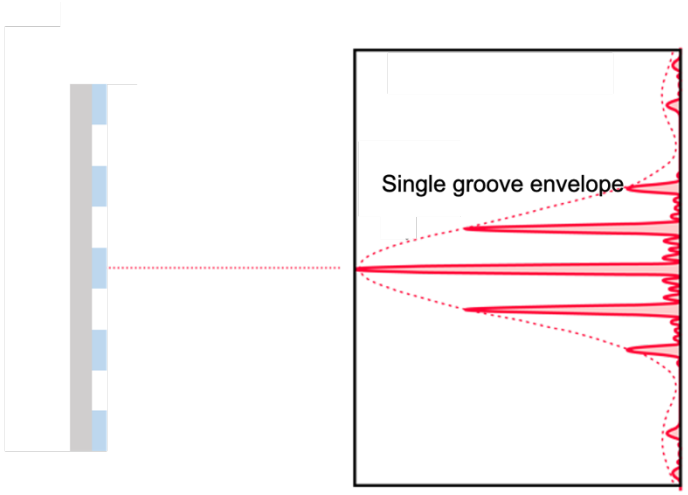

Figure 2.4. The diffraction pattern on (five) reflective gratings.

(Modified from http://hyperphysics.phy-astr.gsu.edu/)

2.2.3 Optical diffraction with illumination at an angle

The aforementioned example only shows the outcome of illumination incidence that is vertical to the grating plane. However, when illuminated at a certain angle, the diffracted light will be directed at specific angles with different diffraction orders (Figure 2.5). The zeroth order diffraction follows the reflection principle, which states that the angle between the incident light and normal is equal to the angle between the reflected light and normal. The angular shift of the other orders of diffraction is determined by the grating periodicity and can be calculated using the following equation:

$$\sin\theta_m = \sin\theta + m\frac{\lambda}{\Lambda} \qquad \text{(eqn. 2.7)}$$

where m denoted as the m^{th} order of diffraction and θ is the angle between the direction of light and normal, λ is the wavelength of diffraction light, and Λ is the grating periodicity. The negative values of m simply mean the diffraction orders are at the same side of incident light with respect to the normal.

This equation (eqn. 2.7) determines the diffracted angle of each color at each order of diffraction, and the result shows the higher order diffractions have wider spectrums and lower saturation than that of the lower orders.

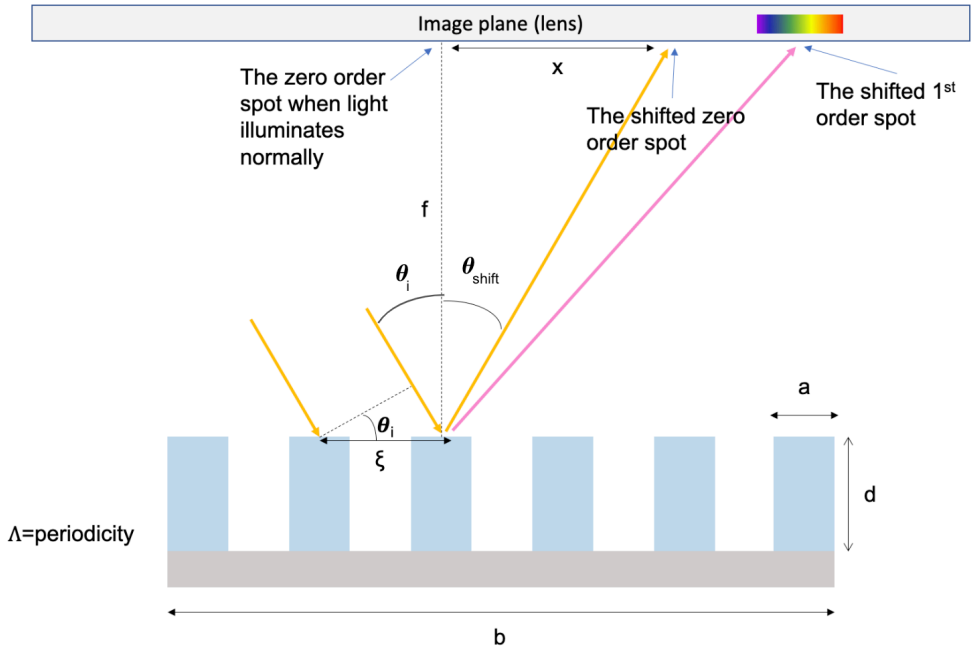

Figure 2.5. The angular shifting of different diffraction orders from the effect of incident light at an angle θ_i

2.3 Optical grating design on OMA

As previously mentioned, Fraunhofer diffraction theory explains that the diffracted image pattern corresponds to the Fourier transformed pattern of the grating structure when the distance (D) between the grating and the image plane is significantly larger than the aperture diameter (d) (D/d >> 64000). However, in practical optical setups, it is often not feasible to have such a large space. Fortunately, a lens possesses the inherent capability to perform Fourier transformation, allowing us to obtain the Fourier transformed image of the grating structure on the image

detector by placing a camera with a lens beneath the OMA platform. This means that the size of the micromirrors and the grating structure on the micromirrors must be carefully designed to achieve an ideal diffracted pattern for measurement. When illuminating a broadband white light on our grating structure, the reflected electric field can be expressed as:

$$E_0 e^{-i0}\left[rect\left(\frac{\xi}{b}\right)\cdot\frac{1}{\Lambda}comb\left(\frac{\xi}{\Lambda}\right)\right] * rect\left(\frac{\xi}{a}\right) \qquad \text{(eqn. 2.8)}$$

where E_0 is the electric field amplitude, ξ is the coordinate at x direction, a is the grating width, b is the micromirror diameter, and Λ is the periodicity of grating structure. Therefore, the corresponding Fourier transformed diffraction patterns can be expressed as:

$$E_0\,[|b|sinc(bv_x) * comb(\Lambda v_x)]\cdot|a|sinc(av_x) \qquad \text{(eqn. 2.9)}$$

where $v_x = \frac{1}{\lambda}\left(\frac{x}{f}\right) = \frac{1}{\lambda}tan\theta_m$ = the x component of spatial frequency.

The relationship between grating structure and Fraunhofer diffracted pattern is shown in Figure 2.6. In consideration of the fabrication tool (ASML stepper), a grating periodicity of 1.2 μm was chosen to ensure a comfortable linewidth (a = 600 nm) for the machine.

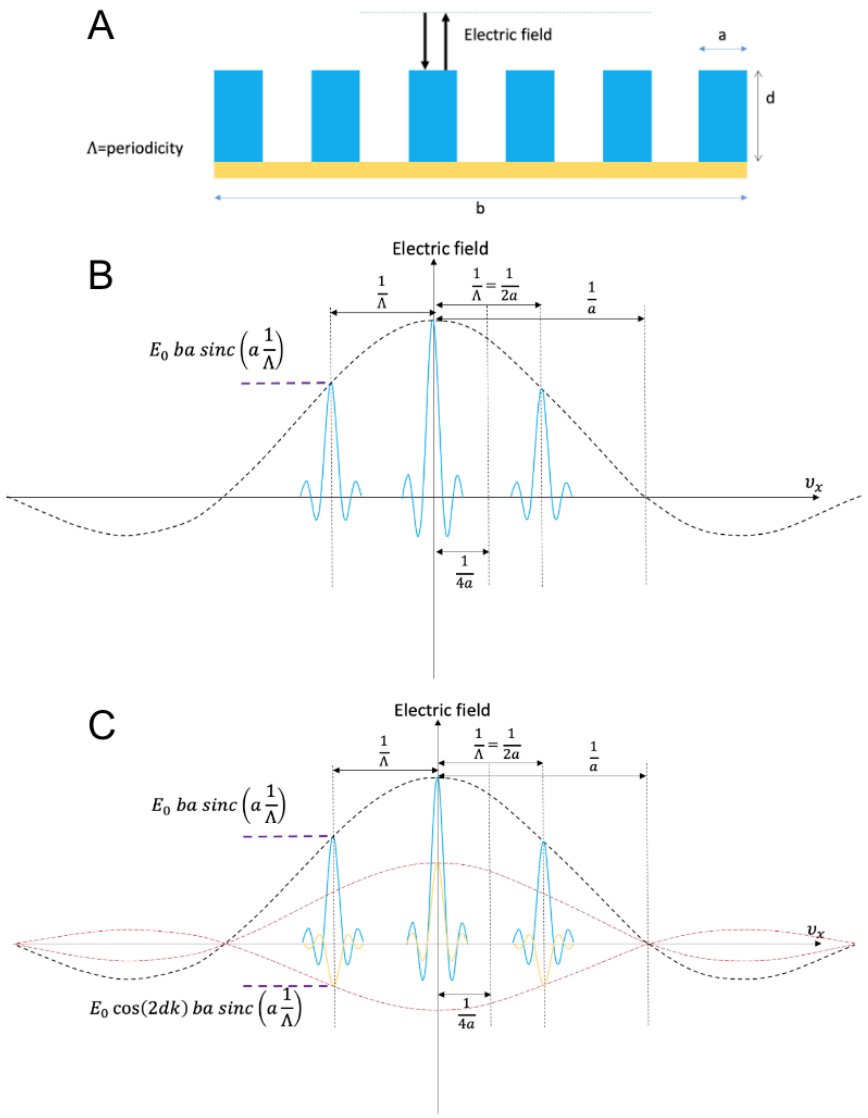

Figure 2.6. The illustration of grating design on OMA device and the corresponding diffraction patterns. (A) The grating structure on the micromirrors, a: grating width, b: micromirror diameter, d: grating depth. (B) The corresponding diffracted profile: the large black sinc function envelop resulting from the grating width and confines the small blue sinc curves originating from the comb and rectangular functions of the grating structure itself. (C) The overall diffracted field profile. The large red sinc curve is the effect from the cos2dk term which confines the profile of the yellow sinc functions from the grating bottom.

2.3.1 Effect of the height of grating

From the analysis above, we can obtain the reflective electric field from the grating top layer (Figure 2.6A, blue part) by simply calculate the Fourier transform of the grating structure. However, the effect of reflectance from the bottom of grating (Figure 2.6A, yellow part) cannot be neglected, which has an optical path shift of the reflected field and will translate into a phase shift in the electric field. The reflected electric field from the grating bottom can be expressed as:

$$E_0 e^{-i2dk}\left[rect\left(\frac{\xi}{b}\right)\cdot\frac{1}{\Lambda}comb\left(\frac{\xi-a}{\Lambda}\right)\right]*rect\left(\frac{\xi}{a}\right) \qquad \text{(eqn. 2.10)}$$

and the Fourier transformed field is:

$$E_0\ \cos 2dk\left[|b|sinc(bv_x)*e^{-i2\pi av_x}comb(\Lambda v_x)\right]\cdot|a|sinc(av_x) \qquad \text{(eqn. 2.11)}$$

The total diffracted electric field is illustrated in Figure 2.6C. Therefore, in order to minimize the reflective field from the bottom, we need to design the grating height by making cos2dk = 0:

$$2d\frac{2\pi}{\lambda}=\left(n+\frac{1}{2}\right)\pi \Longrightarrow d=\frac{2n+1}{8}\lambda \qquad \text{(eqn. 2.12)}$$

In order to have maximum reflectance, we choose Al as the grating material on the micromirrors due to its high reflectivity in the visible light range. Figure 2.7 shows the reflectivity of common metals. Al has higher reflectivity and better uniformity than other commonly used metals such as Au and Ag in the visible light range (400 nm-700 nm).

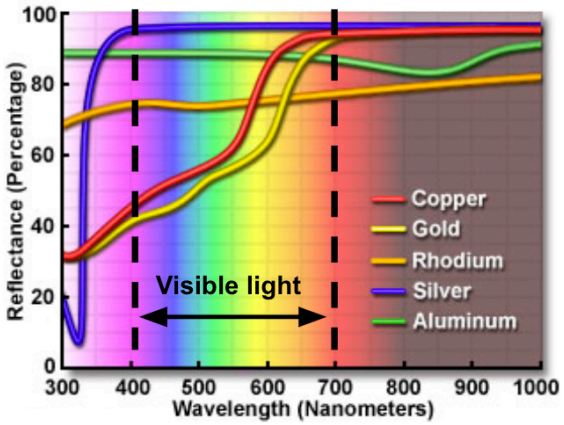

Figure 2.7. The reflectance spectrum of common metals.

Aluminum has high reflectivity in the visible light. (modified from https://www.olympus-lifescience.com/de/microscope-resource/primer/lightandcolor/mirrorsintro/)

2.4 Effect of large FOV device on color variation

The aforementioned illustration only provides an optical analysis of a single micromirror. However, the actual field of view (FOV) for the OMA device encompasses more than 50,000 micromirrors and spans over an area of 5.1 mm × 7.2 mm. Thus, a more precise analysis must be carried out for the entire FOV. As the FOV is considerably large, the micromirrors located at the opposite ends of the device will be subjected to distinct incident angles under the same illumination (Figure 2.8 left), resulting in varying detected colors even if all the micromirrors have the same tilting angle. Hence, the detected colors of the entire FOV will showcase a color gradient from one side to the other. After a uniform magnetic actuation, all the micromirrors will tilt to a certain angle, causing the entire spectrum to exhibit another color gradient with a blue-shift (Figure 2.8 right).

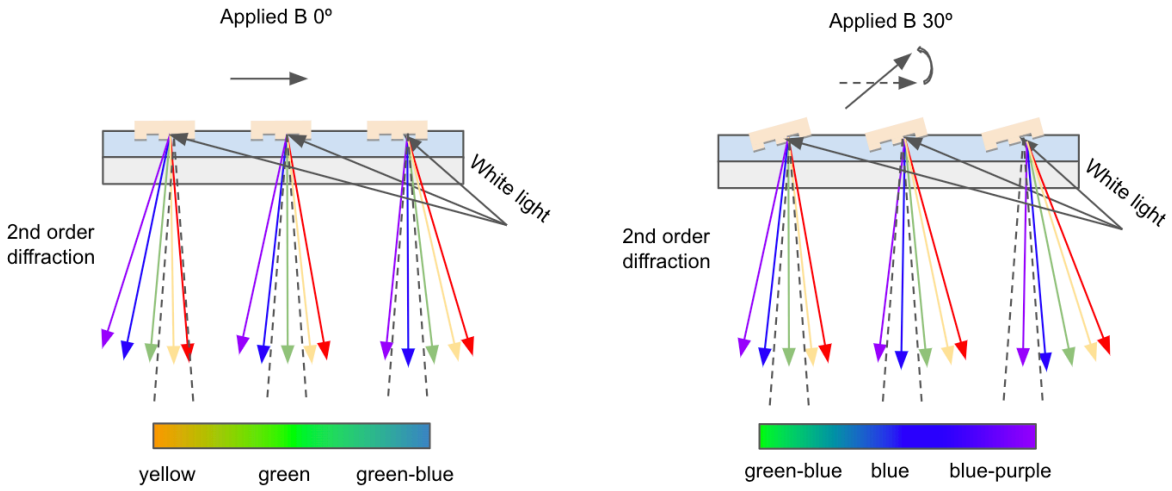

Figure 2.8. The illustration of color spectrum across the entire FOV before (left)/after (right) magnetic actuation. Since the difference of micromirror spatial locations, the distinct illumination and diffraction angle will lead to different detected colors with the same tilting angle for each micromirror.

2.5 Optical setup design

2.5.1 Numerical aperture of camera lens

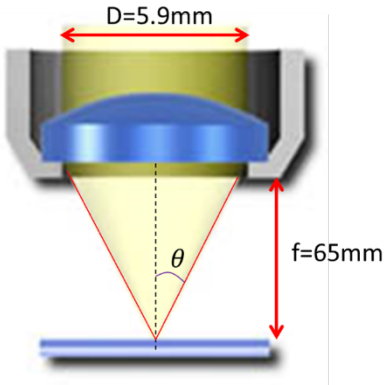

Figure 2.9. Diagram showing the half angle of light entering the lens. f: focal length. D: lens diameter (M. W. Davidson *et al*)

The numerical aperture (NA) characterizes the range of angles over which the system can accept or emit light and is defined as:

$$NA = n \cdot sin\theta \qquad \text{(eqn. 2.13)}$$

where n is the refractive index of the medium in which the lens is working, θ is the maximal half-angle of the cone of light that can enter or exit the lens as Figure 2.9 shows.

In commercial camera lens configurations, the f number (f/# or N), which is the ratio of the system's focal length to the diameter of the entrance pupil, follows the equation:

$$N(or\ f\#) = \frac{f}{D} \qquad \text{(eqn. 2.14)}$$

where f is the focal length and D is the diameter of entrance aperture.

The relations between f# and NA follows the equation:

$$NA = n \sin\theta = n \sin\left[\tan^{-1}\left(\frac{D}{2f}\right)\right] \approx n\frac{D}{2f} = \frac{n}{2N} \qquad \text{(eqn. 2.15)}$$

Thus, a larger f# leads to a smaller NA and smaller aperture for light to come into the lens.

The OMA platform measures cellular biophysical properties by detecting color changes on each micromirror. Ideally, each mirror should represent only one color to facilitate quick distinction. Therefore, we choose a camera lens with a low numerical aperture (NA), or a smaller aperture in the camera configuration, to capture only a small portion of the light spectrum reflected from each micromirror (Figure 2.11). When using a high NA lens, it captures a broad color spectrum band, which reduces the spectrum resolution for tilting angle measurement. Conversely, a smaller NA results in lower light energy entering the camera sensor and lower sensitivity, which creates a trade-off between them. Longer exposure times can increase photo energy but also introduce larger noise from the background or the optical system.

In addition, higher orders of diffraction have a wider spectrum, which allows for collecting a small color spectrum and purer color with a fixed NA lens, but can result in lower saturation. Therefore, a balance must be struck among NA, exposure time, diffraction orders, noise, and sensitivity to optimize the OMA platform's performance.

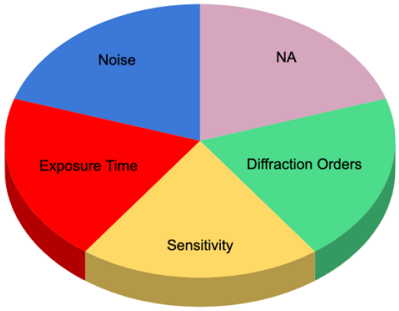

Figure 2.10. The factors contributing to the optical readout on our platforms.

A thoughrou consideration of each factor to balance each other is important to achieve ideal imaging results.

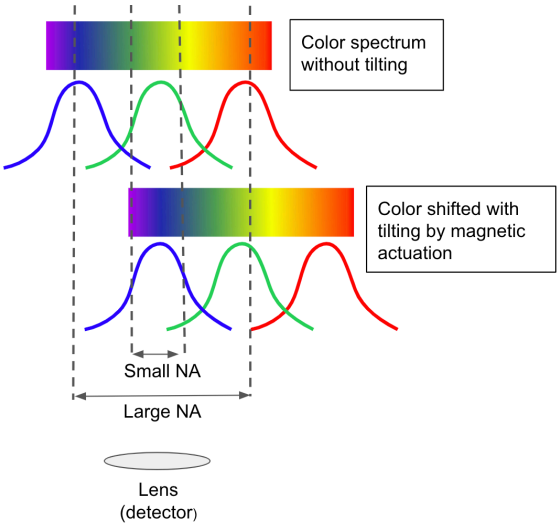

Figure 2.11. The illustration of the effect of different NAs.

An optical system with a larger NA will capture a wider spectrum of diffracted light while a smaller NA can capture a purer color.

2.5.2 Optimization of optical parameters in camera lens system

In order to retain a good sensitivity, we choose camera settings as follows:

F number: f/8, which equals to NA = 1/16

Shutter speed: 1/20 sec, shutter speed controls the time span light can come into the image sensor while capturing the image. At 1/20 sec, it yields a relatively long exposure time but keeps a reasonable signal-to-noise ratio and good intensity

2nd order diffraction: other than 1st order, 2nd order diffraction provides wider spectrum and maintain a sufficient saturation for high sensitivity

2.5.3 Illumination design and result

With the optical diffraction equation above, we are able to calculate the angle between the incident light and the mth order diffraction spectrum:

$$\sin\theta_m = \sin\theta + m\frac{\lambda}{\Lambda} \qquad \text{(eqn. 2.16)}$$

Since we use a camera lens under our OMA platform and we choose the wavelength in the middle of the full spectrum to be 532 nm, the diffracted angle of 2nd order green light can be set as 0º, therefore,

$$\sin 0° = \sin\theta + (-2)\frac{532\ nm}{2 \times 600\ \text{nm}} \qquad \text{(eqn. 2.17)}$$

which makes the illumination angle θ to be 66.44°. by using the same equation, we can obtain the diffracted angle of blue (450 nm) and red light (650 nm) as 9.59° and -9.59° respectively so the full spectrum spans around 20°. On the other hand, when micromirrors tilt with magnetic actuation, the detected color will shift from green color to a bluer range due to the angle between incident light and normal changes. This can be validated by the above equation and shown in the figures below.

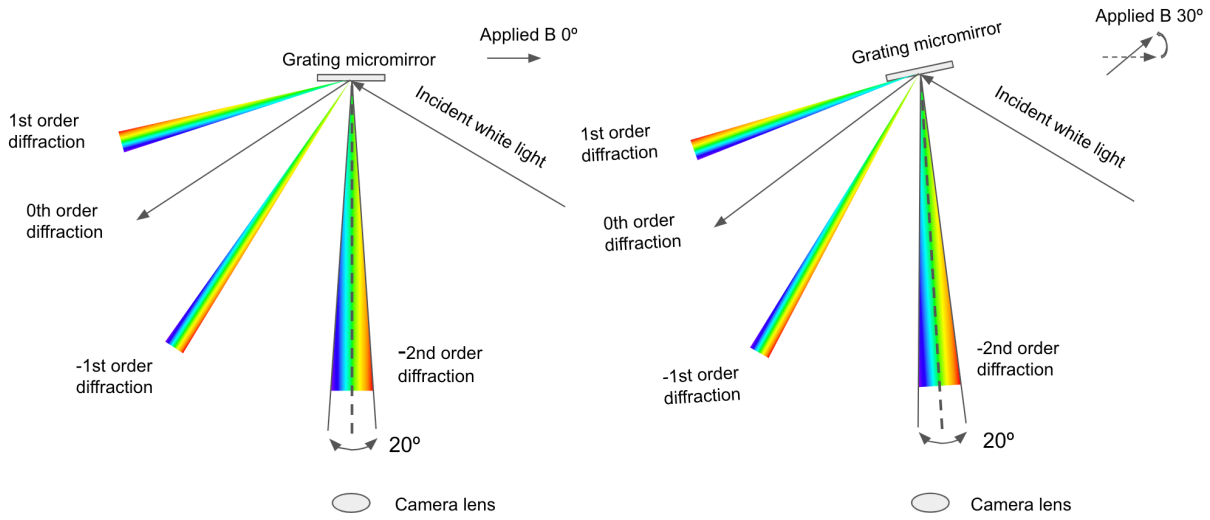

Figure 2.12. The designed incident angle and corresponding diffraction angle of different wavelengths. Left: Optical path and diffraction before magnetic actuation. Right: Optical path and diffraction after magnetic actuation.

The f# we choose yields a NA of 1/16 and half cone angle to be 3.58°, which collects mainly green light from the grating micromirrors when they have no tilt while collect mainly blue light when they tilt by 5° with magnetic actuation.

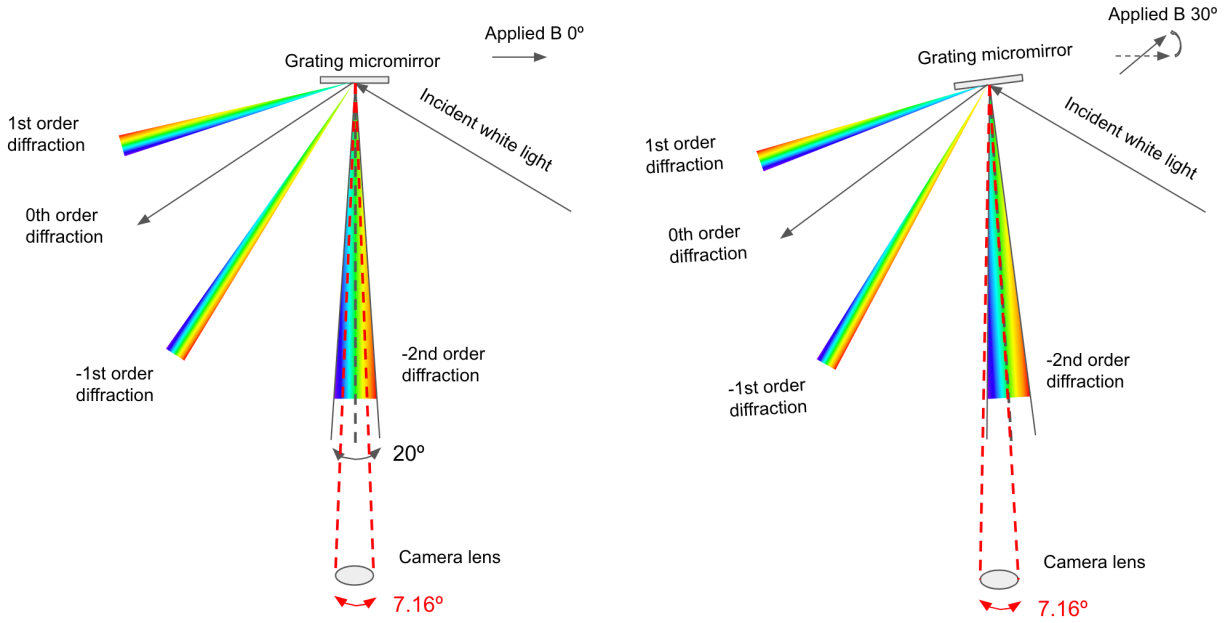

Figure 2.13. The collected angle of 2nd diffraction based on the NA we choose in our camera systems. The diffracted optical path before (left)/after (right) magnetic actuation with collected diffraction light cone 7.16º by the NA (1/16) we choose.

2.6 Magnetism and shape anisotropy

2.6.1 Demagnetizing field

When an external magnetic field is imposed on a magnetic material, the material aligns its magnetization in the direction of the applied field. However, this alignment can produce an internal magnetic field that opposes the applied field, leading to demagnetization. This opposing field is known as the demagnetizing field. The strength and orientation of the demagnetizing field are influenced by the material's geometry and the distribution of magnetization within it (Figure 2.14) [84].

As an example, when a magnetic material is subjected to a magnetic field H_a along both its long axis (Figure 2.14B) and short axis (Figure 2.14C), the saturation of the sample along the

short axis will result in a much larger demagnetizing field H_d compared to that along the long axis. This is why the long axis is often referred to as the "easy axis," since it is easier to saturate. The net magnetic field inside the sample can be obtained by:

$$H_{net} = H_a - H_d \qquad \text{(eqn. 2.18)}$$

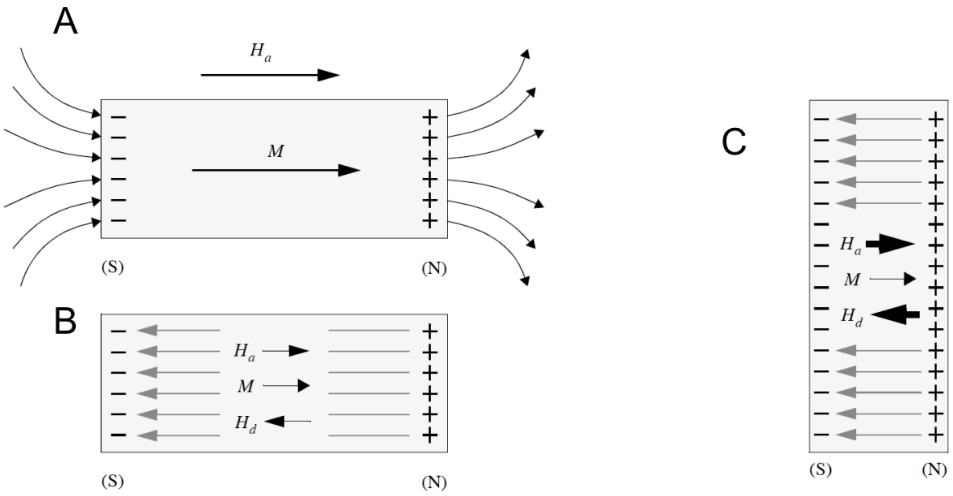

Figure 2.14. Applied magnetic field and demagnetization in a magnetic material.

(A) the illustration of the induced magnetization of a magnetic material in an applied field. (B) the effect of applying a field along its long (easy) axis (C) the effect of applying a field along its short (hard) axis. (Judy, J. W.)

2.6.2 Magnetic shape anisotropy

Magnetic shape anisotropy is a phenomenon in which the magnetic properties of a magnetic material depend on its shape or geometry. It occurs when the shape of a magnetic material is not symmetric, causing the magnetization to be preferentially oriented in one direction over another. For example, an ellipsoid (Figure 2.15) will have a different magnetic behavior compared to a spherical particle of the same material. This is because the elongated shape gives rise to a uniaxial anisotropy, meaning that the magnetization tends to align along the long axis of the shape.

The rotation of the magnetization vector away from the easy axis is determined by a magnetic anisotropy energy that is dependent on material properties and sample geometry. The magnetic anisotropy energy is minimized along the easy axis and dictates the angle of magnetization rotation. A larger total magnetic anisotropy reduces the degree to which the magnetization vector can rotate away from the easy axis for a given magnetic field. This indicates that magnetic anisotropy plays a crucial role in determining the orientation and stability of magnetization in a material.

Figure 2.15A and 2.15B illustrate a magnetic sample with an ellipsoidal shape (2D and 3D respectively) placed in a magnetic field not aligned with the easy axis. The applied magnetic field H_a is at an angle ϕ, and induced magnetization M is at an angle θ to the easy axis.
The induced magnetization M of a multi-domain magnetic material can be expressed as:

$$M = \frac{\mu_0(\boldsymbol{H_c} + \boldsymbol{H_a})}{N_d} \qquad \text{(eqn. 2.19)}$$

where H_c is coercive magnetic field in the object, H_a is the applied magnetic field, N_d is shape coefficient of the object, with $N_d = N_a cos^2\alpha + N_b cos^2\beta + N_c cos^2\gamma$, α, β, γ are the angle between the magnetization and 3 semi-axes of the ellipsoid, and N_a, N_b, N_c are shape coefficients of three axes of the object (Figure 2.15B).

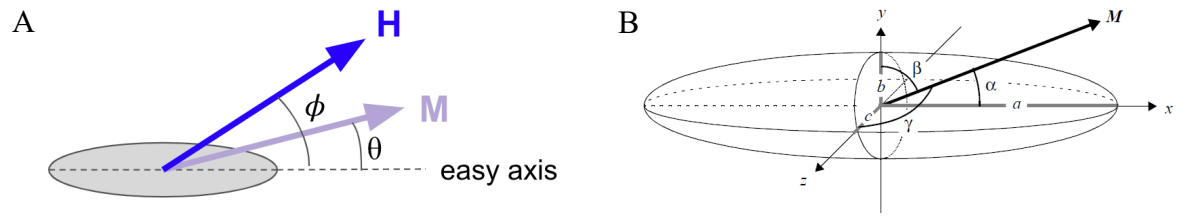

Figure 2.15. The phenomena when an ellipsoid magnetic sample placed in a magnetic field not aligned with the easy axis.

(A) a 2D illustration. (B) a 3D illustration (Judy, J. W.). The magnetization of any magnetic material can be expressed as three shape coefficient and the angle between the induced magnetization M and three axes.

If the applied magnetic field H_a is at an angle ϕ to the easy axis (Figure), by substituting H_a and N_d into Eq. (2.17) we solve for M:

$$M = \min\left(\frac{H_c + H\cos(\phi - \theta)}{\sqrt{N_a cos^2\alpha + N_b cos^2\beta + N_c^2 cos^2\gamma}} \quad , \quad M_s\right) \qquad \text{(eqn. 2.20)}$$

The magnetic-anisotropy energy, denoted as U_a, is minimized when the magnetization vector is aligned parallel to the easy axis. As the magnetization vector deviates from this alignment by an angle θ, the anisotropy energy increases until it reaches a maximum when the magnetization vector is oriented halfway between the current and the next easy axis (θ = 90°). The magnetic shape anisotropy energy is given by

$$U_a = VKsin^2\theta \qquad \text{(eqn. 2.21)}$$

with magnet volume V, magnetic shape anisotropy constant K and the angle θ is the magnetization vector makes with the effective easy axis.

As the magnetization vector deviates from the easy axis, the magnetic anisotropy energy increases, resulting in a restoring torque that aims to realign the magnetization with the easy axis.

The restoring torque can be obtained by differentiating the anisotropy energy with respect to the angle between magnetization direction and easy axis:

$$\tau_{aniso} = -\frac{dU_a}{d\theta} = -VK \sin 2\theta \qquad \text{(eqn. 2.22)}$$

Since the origin of the shape anisotropy in the ellipsoid comes from the demagnetization field, which can be expressed as:

$$H_d = -\frac{N_d}{\mu_0} M \qquad \text{(eqn. 2.23)}$$

The magnetostatic energy density u_{ms} associated with the demagnetizing field of a sample is given by:

$$u_{ms} = -\frac{1}{2}\boldsymbol{H_d} \cdot \boldsymbol{M} = \frac{1}{2}\frac{N_d M^2}{\mu_0}$$

$$= \frac{1}{2}\frac{M^2}{\mu_0}\,[N_a cos^2\alpha$$

$$+ N_b cos^2\beta + N_c^2 cos^2\gamma] \qquad \text{(eqn. 2.24)}$$

If the magnetic field is constrained to xz plane, $\gamma = \pi/2$ and $\cos\beta = \sin\alpha$, the magnetostatic energy density u_{ms} becomes:

$$u_{ms} = \frac{1}{2}\frac{M^2}{\mu_0}\,[N_a cos^2\alpha + N_b sin^2\alpha]$$

$$= \frac{1}{2}\frac{N_a M^2}{\mu_0} + \frac{1}{2\mu_0}(N_b - N_a) M^2 sin^2\alpha \qquad \text{(eqn.2.25)}$$

Neglecting the constant-energy term and using $\theta = \alpha$, the magnetic shape anisotropy energy density can be written as:

$$u_{ms} = \frac{1}{2\mu_0}(N_b - N_a) M^2 sin^2\theta \qquad \text{(eqn. 2.26)}$$

the shape-anisotropy constant K can be expressed as:

$$K = \frac{1}{2\mu_0}(N_b - N_a)M_s^2 \qquad \text{(eqn. 2.27)}$$

2.6.3 Soft magnetic sample in magnetic field

Now we consider the magnetic ellipsoid sample fixed in a magnetic field in which direction is not align with the object's easy axis (Figure 2.16B). For a more universal consideration, we assume the ellipsoid is a multi-domain sample. When an applied magnetic field induces a magnetization with an orientation between the easy axis and the applied field, a driving torque is produced by the applied magnetic field, which can be expressed as:

$$\tau_{field} = VM \times H = VMH\cos(\phi - \theta) \qquad \text{(eqn. 2.28)}$$

with magnetic sample volume V, induced magnetization M and applied field H.

and the shape anisotropy torque will balance out the driving torque at equilibrium and leads to:

$$\begin{aligned} & VM \times H - VK\sin 2\theta \\ =\ & VMH\cos(\phi - \theta) - VK\sin 2\theta = 0 \end{aligned} \qquad \text{(eqn. 2.29)}$$

Equation 2.20 and equation 2.29 can be solved iteratively to obtain M.

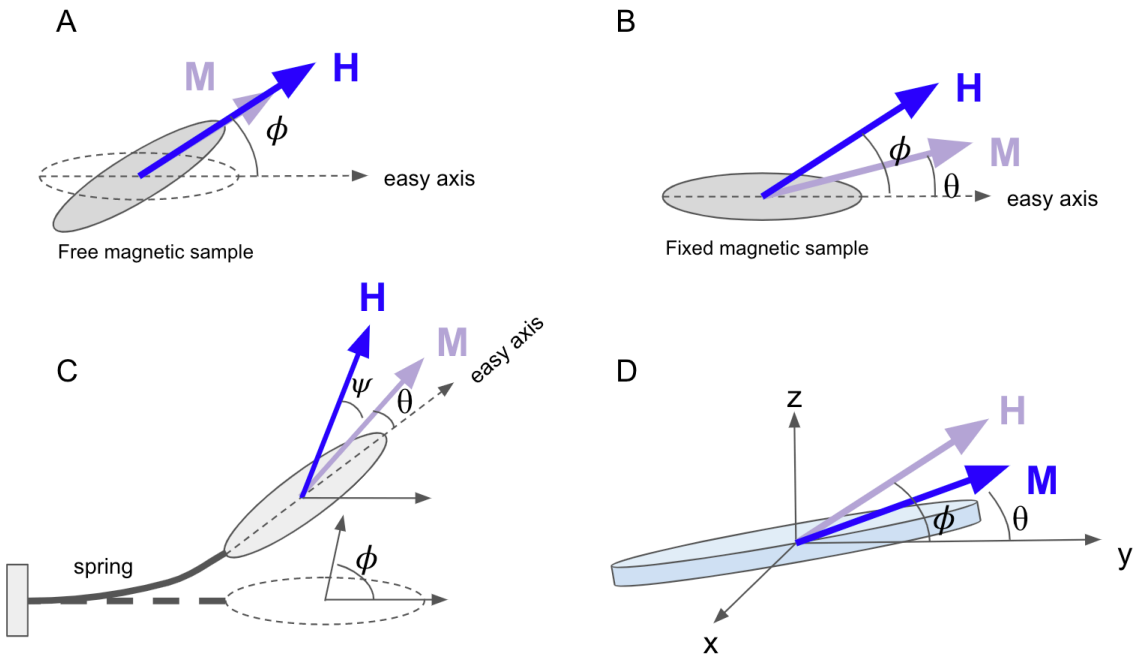

Figure 2.16. Magnetic shape anisotropy on non-symmetric magnetic sample.

(A) A soft magnetic sample free to rotate in an applied field with an angle ϕ with respect to the easy axis. The sample will align the easy axis with the applied field due to shape anisotropy. (B) A soft magnetic sample fixed in an applied field with an angle ϕ with respect to the easy axis. Since the sample is fixed, it will not rotate with the magnetic field but the induced magnetization will lie in between the applied field and the easy axis with an angle of θ to balance out the magnetic torque. (C) A soft magnetic sample connected to a spring in an applied field with an angle ϕ with respect to the easy axis. (D) The shape anisotropy applied in our magnetic micromirrors.

On the other hand, if the object is free in the space, the object will rotate freely until its easy axis aligns with the magnetic field (Figure 2.16A).

However, most of the cases are not that simple. Here is an example of a soft magnetic object connected to a mechanical spring with an angular stiffness k_ϕ rather than fixed (Figure 2.16C) in the space. When a magnetic field is applied at an angle ϕ to the original orientation of the easy axis, the oval object will be subjected to a magnetic torque from the magnetic field:

$$\tau_{field} = VMH \sin(\psi) \quad \text{(eqn. 2.30)}$$

Due to the resistant from the spring, the object will eventually stop and reach at equilibrium at a position between the original orientation and the applied field.

When the magnetization vector deviates from the easy axis by an angle θ, the anisotropy torque T_{aniso}, which acts between the magnetization vector and the easy axis, increases in response to the rotation. This increase in T_{anis} counteracts the driving torque and results in a restoring torque that aims to realign the magnetization with the easy axis:

$$\tau_{aniso} = -VK \sin 2\theta \quad \text{(eqn. 2.31)}$$

Since the spring is bent by the exerted magnetic torque, there is a mechanical restoring torque to counteract to the shape anisotropy torque:

$$\tau_{mech} = -k_{\phi}\phi \quad \text{(eqn. 2.32)}$$

And in equilibrium, the net torque on the magnetization and that on the magnetic object is balanced out:

$$\tau_{field} + \tau_{aniso} = 0 \quad \text{(eqn. 2.33)}$$

$$-\tau_{aniso} + \tau_{mech} = 0 \quad \text{(eqn. 2.34)}$$

2.6.4 Magnetic shape anisotropy applied in OMA

In our setup, the micromirrors are circular disks. Therefore, the shape anisotropic property only manifests in the out-of-plane direction (z direction in the Figure 2.16D). When a magnetic field is applied parallel to the OMA device, it is also parallel to the micromirror plane, and the induced magnetization aligns with the long axis of the easy plane. As the magnetic field

H is rotated to a certain angle, the direction of the induced magnetization M lies between the applied field H and the micromirror plane. Consequently, the micromirrors tilt out of plane due to the induced magnetization, which is in line with the shape anisotropy. This can be referred to an example of the ellipsoid magnetic sample connected to two springs on the opposite sides (PDMS for our case).

From equation, the real induced magnetization of our micromirrors can be expressed as:

$$M = \min\left(\frac{H_c + H\cos(\phi - \theta)}{\sqrt{N_a cos^2\theta + N_b cos^2(90° - \theta) + N_c^2 cos^2\frac{\pi}{2}}} \quad , \quad M_s\right) \qquad \text{(eqn. 2.35)}$$

where M_s is saturated magnetization.

2.7 Magnetic torque for actuation

Based on the magnetic shape anisotropy principle and magnetic torque theory, we can calculate the induced magnetic torque on our micromirrors by:

$$\tau_{field} = V\boldsymbol{M} \times \boldsymbol{H} = VMHsin(\phi - \theta) \qquad \text{(eqn. 2.36)}$$

where V is the volume of the object, M is the induced magnetization of micromirrors and H is the applied magnetic field strength.

The magnetic material we choose is cobalt, which provides strong magnetization and also material stability. So now we need to decide how much the magnetic torque we need to actuate the micromirror tilting to 5°. However, before we obtain this information, we need to consider several factors:

1. Young's modulus of the PDMS substrate: the stiffness of the PDMS substrate will determine how large the tilting angle we will have with a fixed torque applied on the micromirrors, which is similar to the spring constant in the case of ellipsoid magnetic sample connected to a spring.
2. The induced magnetization of Co micromirrors: this factor is determined by the material properties, volume, or thickness of the micromirrors and also the magnetic field we apply.
3. Magnetic field flux density B: We need a proper magnetic field generator which can generate a strong and uniform field. However, such an equipment must be large, so we need to consider the size and space constraint of our setup and whether to choose permanent magnets or electromagnets for our source of magnetic field.

With the analysis presented in Section 2.6, the same equations can be applied to calculate the magnetic field, magnetization, and magnetic torque of Co micromirrors. However, determining the effective spring constant of PDMS is not a straightforward process using the approach outlined in Section 2.6. Furthermore, the induced magnetization cannot be calculated simply by assuming that the magnetic properties of Co are equivalent to those discussed above. Therefore, it is impractical to solve the induced magnetization and the driving magnetic torque numerically.

Herein, we use the modeling software, COMSOL, to simulate our situation and use it as a guide to help us decide each of these factors. Before performing simulation, we preliminarily calculate the magnetic torque we need by assuming some parameters to better decide how much magnetic field we need and what the PDMS substrate Young's modulus need to be:

1. A 0.2 T Magnetic field applied at an angle of 30° with respect to micromirrors' easy plane
2. The induced magnetization of cobalt micromirrors will be around 100 emu/g based on the reference [85]
3. With such a magnetic field, the resulting magnetic torque is around 1.05×10^-12 N-m by using Equation 2.36. Here we assume M is aligned with the micromirrors' easy plane (this assumption will result in a larger estimated torque value but within a reasonable range)

In the COMSOL simulation, the Young's modulus of the PDMS substrate was set to 21 kPa, and the Co micromirror thickness was set to 150 nm. The result shows such a torque will be sufficient to generate a tilting angle of 11.8º, which is sufficient for our application (Figure 2.17).

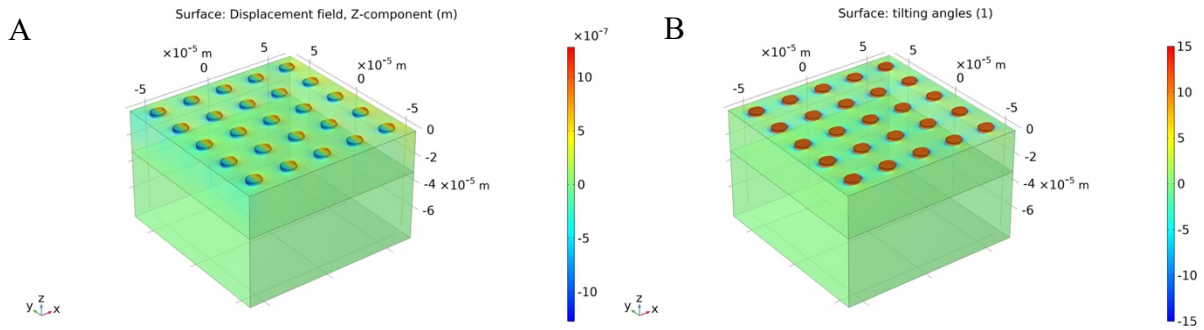

Figure 2.17. Simulation result in COMSOL under an applied magnetic field of 0.2 T at a 30º angle to the easy plane of micromirrors.

(A) Displacement (deformation) in vertical (z) direction. (B) The tilting angle of micromirrors is 11.8º.

2.8 Magnetic setup design

In the OMA platform, uniform actuation of micromirrors is important for optimal device performance. Therefore, ensuring the creation of a uniform magnetic field across the entire device is critical in order to achieve uniform tilt of every micromirror and ensure that each one experiences the same magnetic field strength, denoted as B.

Neodymium Rare Earth (N52 grade) permanent magnets (K&J Magnetics, BX8X8X8-N52) were chosen to generate the required large magnetic field (645.1 mT surface field). A magnet holder was designed and 3D-printed to hold two such magnets at a certain separation. The dimensions of the magnets (1.5×1.5 ×1.5 inches) were chosen to be much larger than the device dimensions (5 mm × 7 mm) to ensure uniform magnetic field throughout the device positioned in between these two magnets.

To determine the distance between the two magnets required to achieve the necessary magnetic field strength, we employed COMSOL to simulate the magnetic field between two N52 magnets using parameters provided by the manufacturer. The simulation (as shown in Figure 2.18) indicates that when the magnets are 2.25 inches apart, they generate a magnetic field of 210 mT at the center between them.

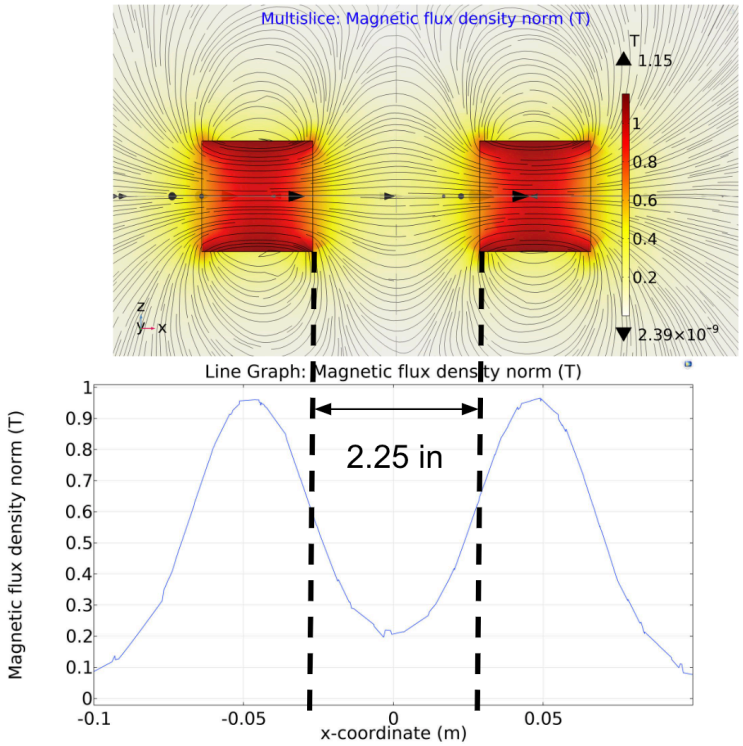

Figure 2.18. The simulated magnetic flux density between two N52 magnets in a separation of 2.25 inches.

To validate the strength and uniformity of the magnetic field, we placed the two magnets in a 3D printed holder separated by 2.25 inch apart and conducted a magnetic field measurement using a Gaussmeter probe. As shown in Figure 2.19, the measurement indicates that the magnetic field at the center between the two magnets is 211.3 mT, with a magnetic field variation within 0.88% in a 7 mm range (the largest dimension of our device) in y direction, and 1.36% and 0.64% in a 5 mm range in x and z direction respectively. These experimental results confirm that this system can create a sufficiently strong and uniform field distribution to actuate the micromirror array positioned in the middle between these two magnets.

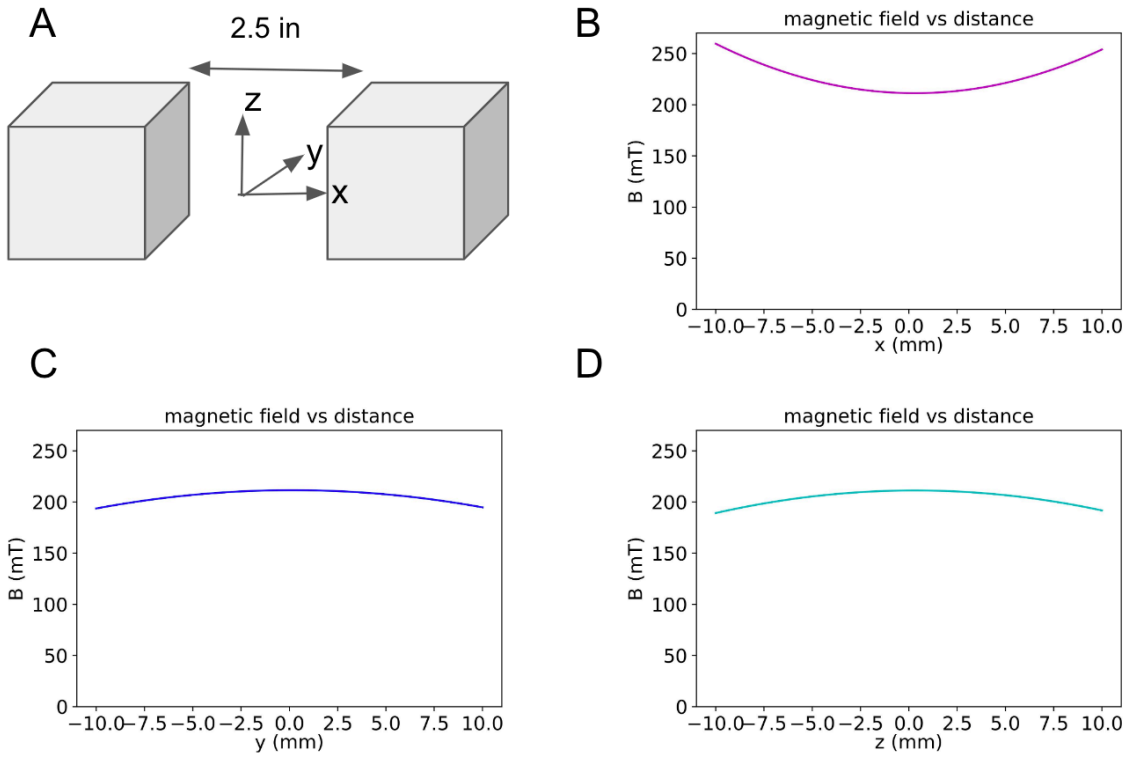

Figure 2.19. Experimentally measured magnetic field data between the two N52 magnet at a 2.25 inches separation. (A) illustration of the magnet set with a 2.25" separation. (B)(C)(D): the magnetic field distribution in the x, y, and z directions respectively show negligible variation within the spatial range (5 mm × 7 mm × 2 mm) of our device.

To induce out-of-plane tilt of micromirrors through magnetic field rotation, we need to rotate the pair of magnets along with the holder. To achieve this, we have designed a rail system that connects the magnet holder and enables radial rotation with respect to the center of the OMA device (Figure 2.20). This design allows the device to be positioned at the center between the two magnets while rotating.

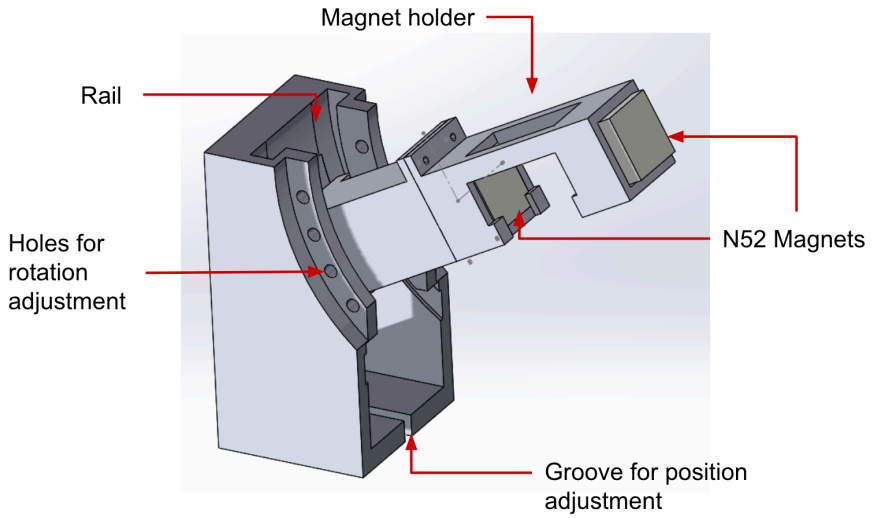

Figure 2.20. The magnetic setup designed for optimal positioning of magnets.

This design enables translational and radial movement (with the rail and groove). The setup consists of a rail system and a magnet holder, ensuring a uniform magnetic field distribution.

2.9 Optical and mechanical decoupling

Since an OMA chip has a periodic array of more than 50,000 micromirrors, before we perform biomimetic tissue stiffness measurement, we need to verify if the coupling effects, both optical and mechanical, between neighboring micromirrors are small and negligible.

2.9.1 Mechanical decoupling

It is important to consider mechanical coupling between micromirrors on a PDMS substrate when they are actuated by magnetic field rotation. Due to the limitations of experimental validation, we used COMSOL simulation to investigate this phenomenon. Specifically, we simulated the tilting angle of a Co micromirror, surrounded by neighboring Si

micromirrors with a pitch of 26 µm, under the magnetic torque applied in the experiment. This approach allows us to calculate the amount of tilting angles induced by a neighboring micromirror. Our simulation results demonstrate that when the center Co micromirror is tilted by 5.24°, the adjacent micromirrors are tilted by only 0.02°, representing less than 0.5% of the center tilt (Figure 2.21). This confirms that there is a negligible mechanical coupling effect between neighboring micromirrors during magnetic actuation.

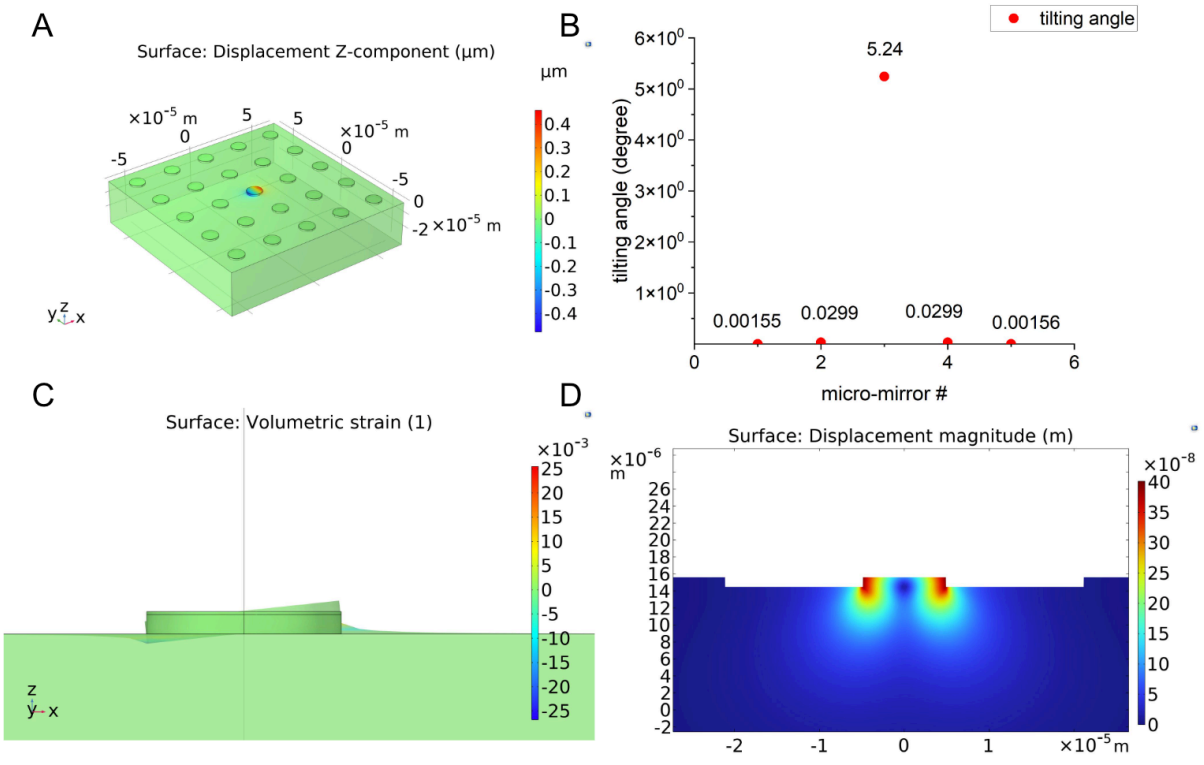

Figure 2.21. Mechanical decoupling of micromirror tilting in COMSOL simulation

(A) PDMS Deformation (z direction) caused by the magnetic torque applied only at the center micromirror (B) The tilting angle data shows that the neighbor micromirrors are affected by < 0.5% of that of the center mirror (both graphs show the middle row of micromirrors). (C) The volumetric strain plot shows that the deformation caused by one micromirror will only affect the area with small proximity. (D) The displacement magnitude remains minimal when it is away from the vicinity of the micromirror.

2.9.2 Optical decoupling

The camera lens collects light within a specific cone angle defined by the numerical aperture (NA) we use. As mentioned earlier, we select a small NA to capture a narrow color spectrum from each micromirror. However, it is important to consider the possibility of optical coupling between neighboring micromirrors, which could potentially impact the color observed on each micromirror. To investigate this, we fabricated the micromirrors with a designed pitch of 26 μm, based on the results of the mechanical coupling simulation. Figure 2.22A illustrates a single micromirror and its neighboring micromirrors, and it clearly shows that there is little coupling, here we mean the images of individual micromirrors do not overlap, observed between them. In addition, we employ image processing techniques to extract the pixel intensity of each micromirror, and upon analysis, we observe a clear distinction between the peak values of the red, green, and blue channels (Figure 2.22B-D).

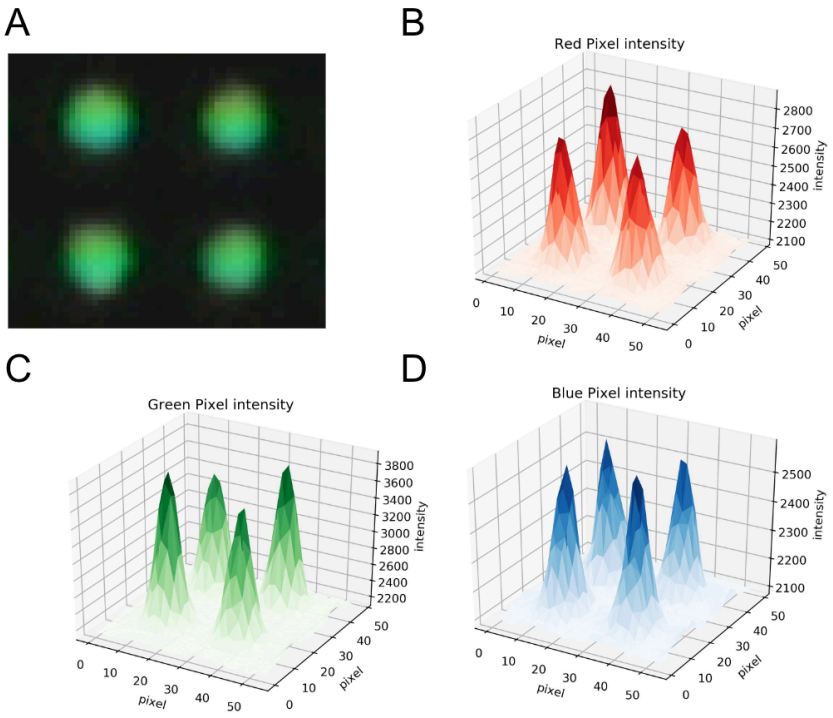

Figure 2.22. Illustration of optical decoupling.

(A) the original image of 4 micromirrors shows clear dark spacing between each micromirror. (B)(C)(D): the red, green, and blue channels of the pixel intensity in the image show there is no optical coupling between each micromirror.

2.10 Optical calibration for color-to-tilt conversion

To quantitatively extract pixel data from the camera (Canon 5D Mark IV), a numerical index must be assigned to each color. The widely used HSV (hue, saturation, value) system is employed, as it separates hue from saturation and brightness, mitigating color matching issues under varying lighting conditions. The image sensor of the camera is equipped with a Bayer filter arranged in a common red, green, and blue pattern (Figure 2.23A), with each pixel collecting the intensity of a single color.

Given that the color sensors are spatially arranged in a periodic pattern, the pixel intensity of each micromirror is inherently dependent on its spatial location (as illustrated in the Figure 2.23B). To accurately represent the color associated with each individual micromirror, we employ a Gaussian fitting algorithm to model the pixel intensity data collected from the red, green, and blue color channels, respectively. This methodology enables us to discern the precise color of each micromirror, while also mitigating the issue of pixel intensity variation within individual micromirrors.

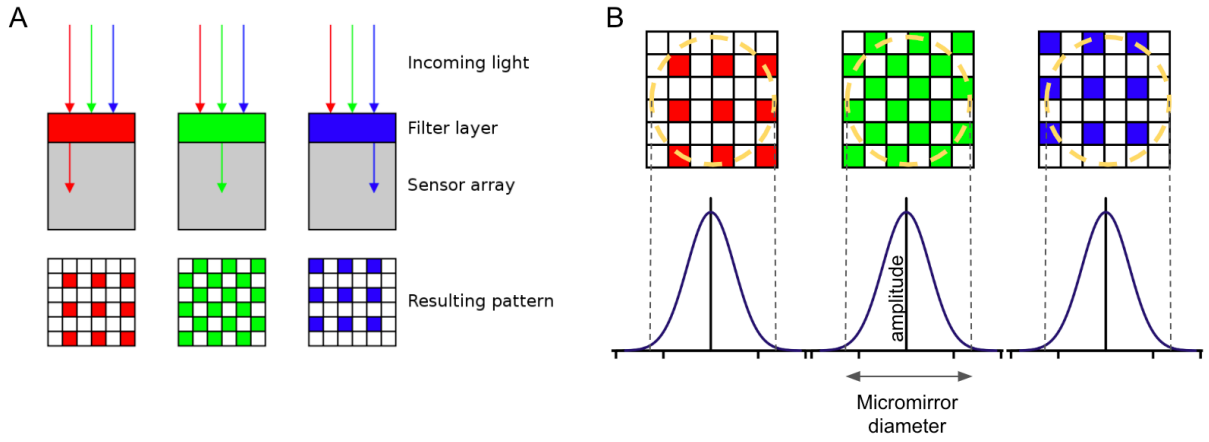

Figure 2.23. Illustration of Bayer pattern filter and Gaussian fitting of the pixel intensity.
(A) The image sensor in the camera applies a Bayer filter, which leads to a spatial arrangement of each color filter. (B) The application of Gaussian fitting can help extract the peak value of each color channel as the representative color component of the micromirror.

As mentioned above, micromirror color varies with locations and tilting angles, which means we must develop an approach to construct the relationship between color and tilt at each location.

Here, we develop a method to perform optical calibration of the OMA device and convert hue values to corresponding tilting angles at each location within the camera field of view

(FOV). The method involves the use of a goniometer stage (Figure 2.24) that allows radial rotation with a fixed radius relative to a rotation center. The goniometer is connected to a 3D printed device holder where the OMA device is inserted. The dimension of the device holder is carefully designed to match the rotation radius of the goniometer so the device will be placed at the rotation center plane. The device holder is then aligned with the camera FOV to overlap the geometrical center of the device holder with the center of the camera FOV. Since each micromirror on the device may have different initial tilting angles due to fabrication variation, we need to pick up a specific micromirror at the center of the FOV as our calibration baseline. This will allow the chosen micromirror to be at the radial center of the goniometer rotation. The goniometer is used to rotate the calibration device between -5°~+5°. Images of the device are recorded at chosen angles between -5°~+5°, and the same steps are repeated at 9 different locations (Figure 2.25G) within the FOV by moving the device horizontally with translational stages. This process results in a dataset of calibration images that is then used to construct the relationships between tilting angles and hue on random locations within the FOV via curve fitting models.

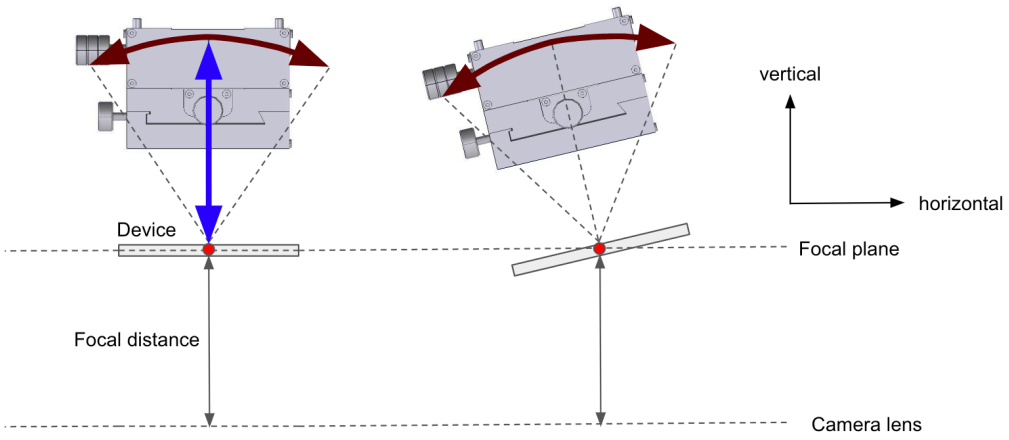

Figure 2.24. The approach of using a goniometer to perform optical calibration.

By aligning the goniometer with the camera and positioning the selected micromirror at the center of the field of view (FOV), we can achieve radial centering of the micromirror during the rotation of the goniometer. This ensures precise calibration and alignment between the goniometer, camera, and micromirror.

The acquired images from the calibration experiment were computationally processed through Gaussian fitting to extract the x and y coordinates and HSV values of the grating micromirrors in focus at the focal plane. To derive a relationship between tilting angles and hue values, we employed the B-spline curve fitting model (multivariate adaptive regression spline, implemented using PyEarth) to fit a hyper surface equation to the extracted data points. Figure 2.25A-C depict the relationship between hue, saturation, and tilting angles of the selected micromirror at 3 different spatial positions within the FOV (red marks in Figure 2.25G), while Figure 2.25 D-F shows the relationship between tilting angles and hue of the chosen micromirror at those 3 locations of the FOV. The white circles in Figure 2.25A-C represent the calibration data obtained from the calibration experiment, while the gradient of the fitted background curve is generated from the PyEarth curve fitting model. Notably, the fitted background gradient exhibits a hue shift at different locations along the illumination direction due to the effect of

large FOV device illustrated in Figure 2.8, and no significant hue shift in the transverse direction with respect to the illumination LED. The curve fitting model was further applied to generate the calibration datasets of the relationship between hue, saturation and tilt across the entire FOV based on the data from those 9 locations (Figure 2.25G). This methodology enables the extraction of tilting angle data converted from hue data at various positions within the FOV for future experiments.

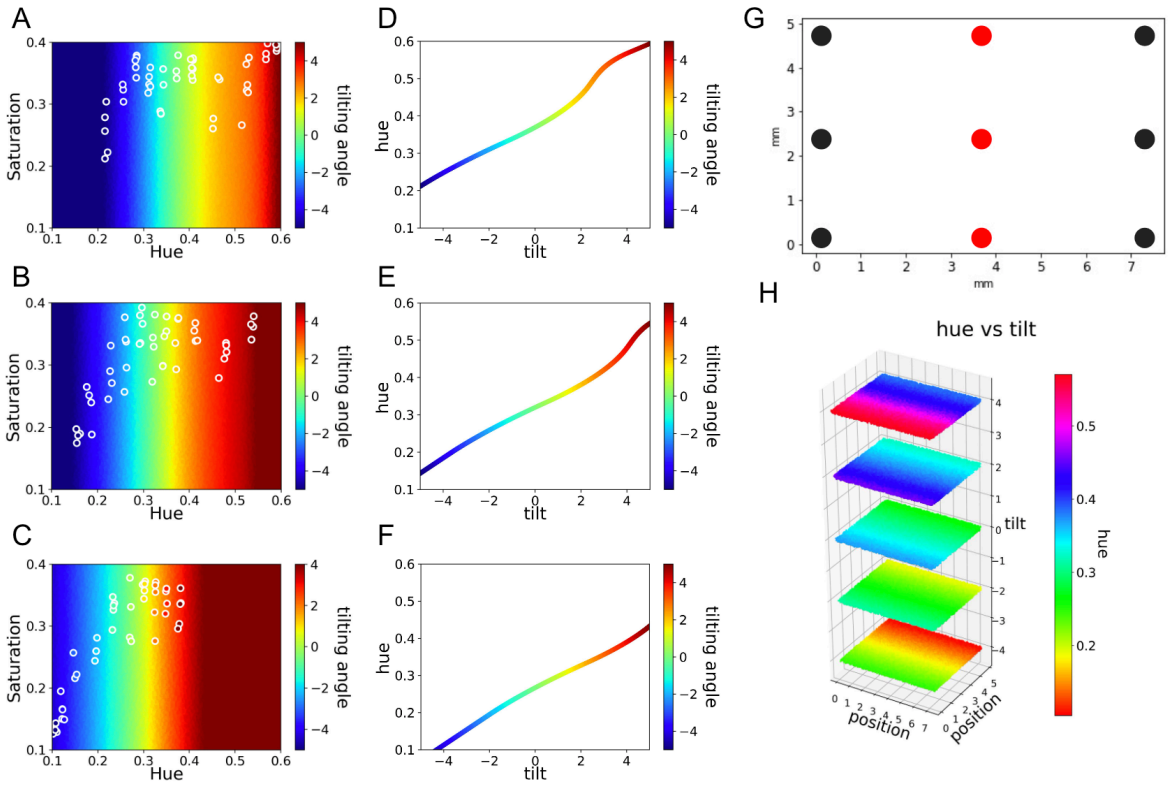

Figure 2.25. Optical calibration result on the entire FOV of device.

(A)-(C) the relationships between hue, saturation and tilting angle of the micromirror at 3 different locations (the red positions in G) White circles represent the experimental data taken from calibration experiment, and the fitted background is generated from fitting model PyEarth. (D)-(F): the relationships between hue and tilting angle of the micromirror at the 3 different locations (the red positions in G). (G) the 9 positions on the entire FOV for optical calibration experiment. (H) the relationships between hue and tilting angle of the entire FOV (5.1 mm × 7.2 mm), generated from the curve fitting model PyEarth.

2.11 Complete setup design

The complete setup is a combination of magnetic and optical setups which includes the following components (Figure 2.26):

1. LED light source (Citizen CLU550-3626C1): We use a power supply to control the LED intensity by setting the current at 2A.
2. Lens (Canon MP-E 65mm f/2.8 1-5x Macro Photo lens): We set the lens at 5x magnification to capture high resolution images.
3. Camera (Canon EOS 5D Mark IV): The configuration is set at manual mode to capture pure raw images, aperture at f/8, shutter speed = 1/20 sec, ISO = 400, Color temperature = 5000K.
4. XY Translation motorized stages (Thorlabs PT1-Z8): two translation stages for controlling x and y position of the device holder with micron scale precision.
5. Goniometer (Misumi): the goniometer is able to rotate between -15~15 degree with 0.1 degree resolution.
6. Device holder (Solidworks designed, 3D printed): It is designed to place a 72 mm×25mm glass slide of the MSPOT device.
7. Magnets (K&J Magnetics, N52), holder and rail for rotation (Solidworks designed, 3D printed)
8. Integration of other plastic components and metal post: To build up the whole system and integrate each parts mentioned above, we use a lot of metal posts, bread boards and 3D-printed parts to meet our need.

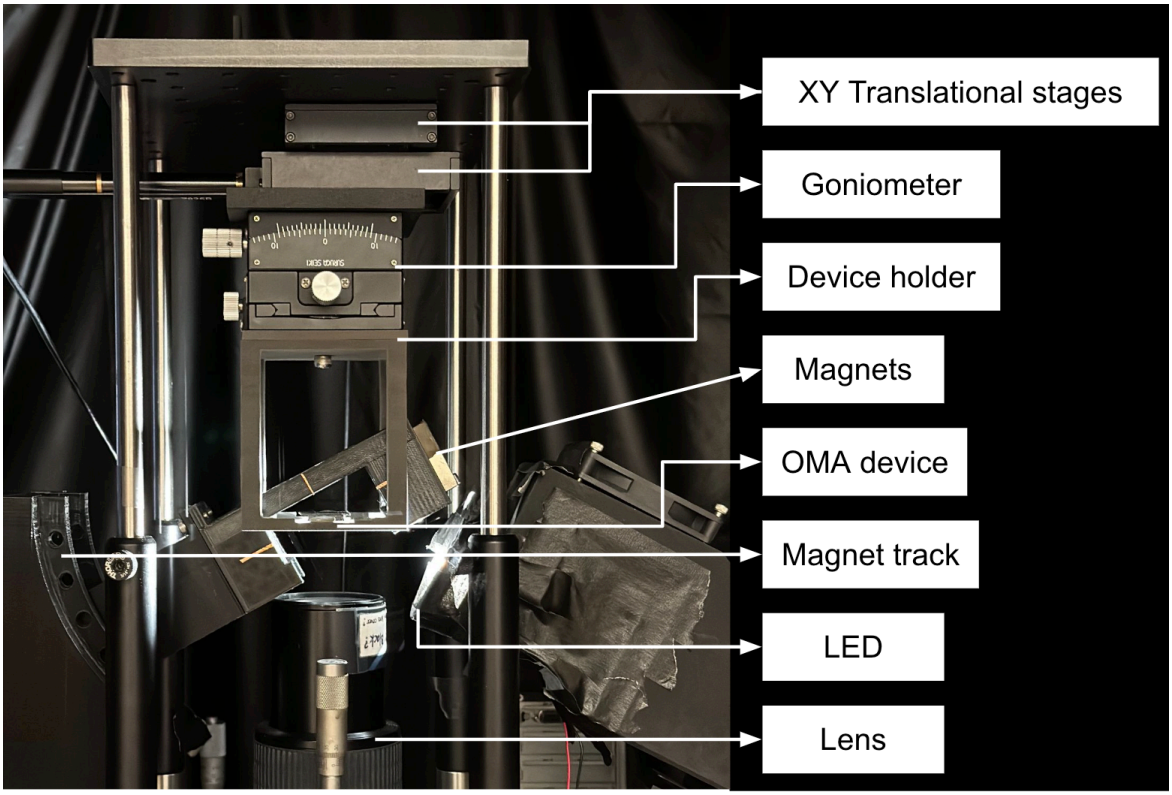

Figure 2.26. The full setup for imaging OMA platform.

2.12 Magnetic actuation result

Figure 2.27A shows the OMA device prior to magnetic actuation, while Figure 2.27B displays the device following a 30° rotation of the magnetic field. It is evident from the image that the micromirrors undergo a blue shift resulting from magnetic torque induced by shape anisotropy. The field of view of the camera utilized in our device is relatively large, measuring 5.1 × 7.2 mm, resulting in a color variance among the micromirrors from one end of the device to the other due to differences in illumination incident angles at various locations (Section 2.4). The image shown is approximately 5 × 5 mm by cropping out the defect area due to fabrication imperfection.

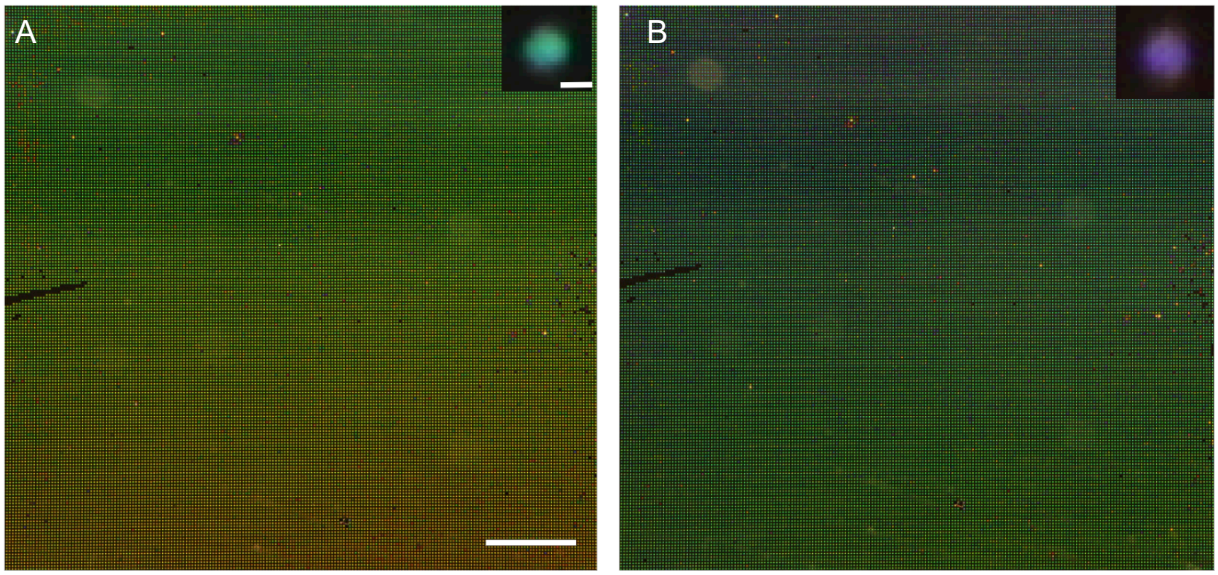

Figure 2.27. The images of OMA device.

Before (A) and after (B) magnetic actuation, showing a field of view of 5×5 mm. Inset, top right: individual micromirrors. Scale bars: bottom right: 1 mm, inset: 10 μm. (Note: periodic artifacts could show up when using an electronic display to view these images at low resolutions. These artifacts disappear when you zoom-in and enlarge these images)

To quantify the change in tilting angle before and after magnetic actuation, we utilized the calibration dataset and curve fitting model to analyze our experimental results. For the actual device measurement, we recorded images and used Gaussian fitting to determine a representative HSV value for each micromirror, following the same approach as the calibration experiment. However, this process was performed on all the micromirrors across the entire FOV, rather than just the selected micromirror used in the calibration experiment. Therefore, it will generate a dataset of the HSV values for all the micromirrors. Figure 2.28A shows the hue data plot of the device before magnetic actuation, while Figure 2.28B shows the hue plot of the device after magnetic actuation, where each data point represents one micromirror.

In order to quantify the tilting angle change, we apply the calibration datasets to convert all the hue data to tilting angle data, which yields a complete dataset of tilting angles for each micromirror. Figure 2.29A shows the tilting angle plot of all the micromirrors within the FOV before magnetic actuation, while Figure 2.29B shows the tilting angle plot of that after magnetic actuation. Figure 2.29C shows the result of tilting angle difference across the entire FOV, which demonstrates a uniform tilting angle change Δt. The average tilting angle change Δt_a is 3.33° and the standard deviation is 0.51º.

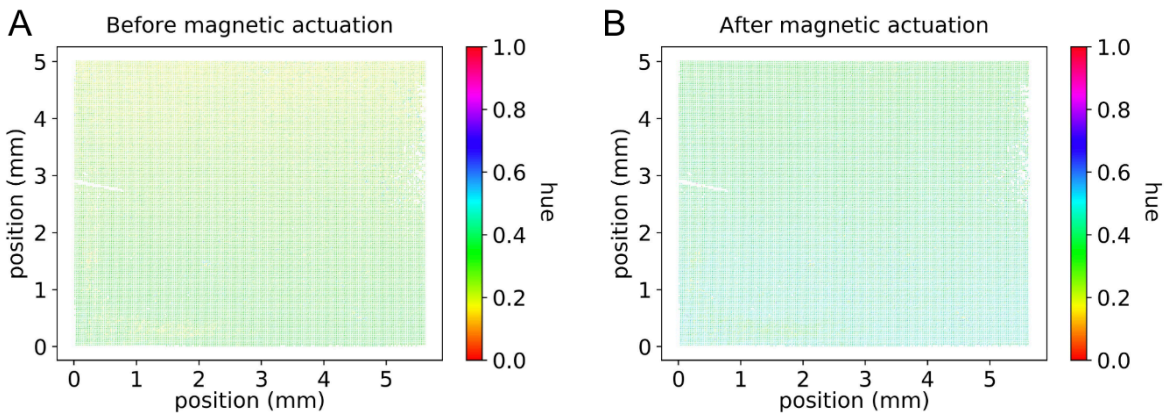

Figure 2.28. The hue on the entire FOV on OMA device after performing Gaussian fitting.

A: The hue plot before magnetic actuation. B: The hue plot after magnetic actuation

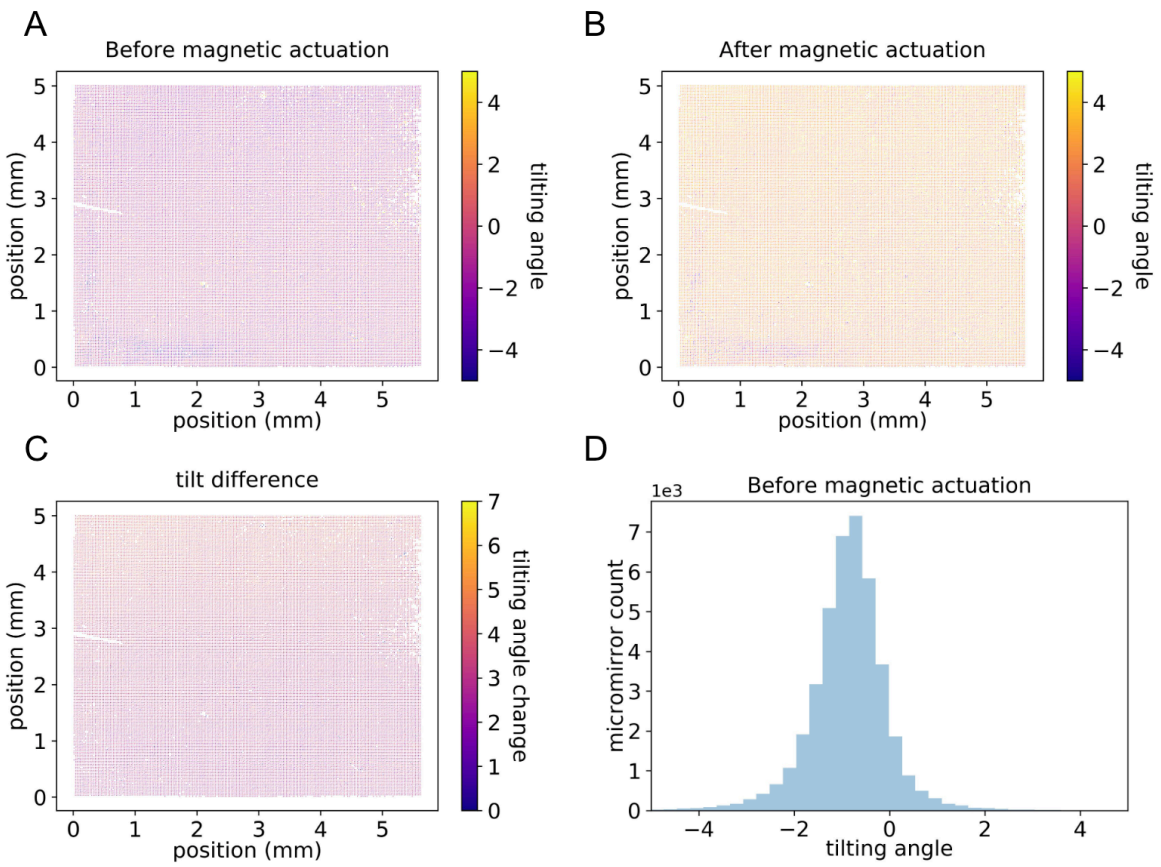

Figure 2.29. The tilting angle on the entire FOV on OMA device after performing optical calibration. (A) The tilting angle plot before magnetic actuation. (B) The tilting angle plot after magnetic actuation. (C) The tilting angle change of the micromirrors. (D) Histogram of initial tilting angle before magnetic actuation.

2.12.1 Impact of initial tilt on magnetic actuation

Due to fabrication variations, not all micromirrors have the same initial tilting angles when a magnetic field is not present. This variation in initial tilting angles can affect the magnetic torque for each micromirror when a magnetic field is applied to actuate them, as the angle between the magnetic field and magnetization will differ. Thus, we conducted an investigation to determine the extent of this impact on the resulting magnetic torque.

Figure 2.29D displays the initial tilting angle plot of the OMA device. The average initial tilting angle is -0.86°. To assess the overall distribution of micromirrors, we generate a histogram of initial tilting angles and determine that the 10th and 90th percentiles are -1.78° and 0.00°, respectively, resulting in a torque variation of 1% when compared to the average tilting angle (by using equation 2.36, assuming M aligns with the micromirror plane). This result confirms that the magnetic torque variation from initial tilting angle is tolerable.

2.13 Fabrication

The OMA devices were fabricated using the following steps. First, a silicon wafer with a 1 μm thermal silicon dioxide layer was used, and a grating structure was patterned onto the thermal dioxide layer using photoresist (SPR700) and stepper photolithography (ASML PAS 5500/200) and dry etching (STS MESC MULTIPLEX AOE). The photoresist (SPR700) was removed using oxygen plasma (Matrix 105 Photoresist Stripper).

Next, the thermal silicon dioxide was patterned with photoresist (KLT 5315) and exposure machine (Karl Suss MA6 aligner) and etched into isolated disks with a diameter of 10 μm (Figure 2.30B). Following disk patterning, the Si layer underneath was further etched down to suspend the disks by using isotropic etching, with the photoresist (KLT 5315) used in the prior etching serving as an etching mask for isotropic reactive ion etching of silicon (Figure 2.30C). After removing the photoresist using oxygen plasma (Matrix 105 Photoresist Stripper), a composite metal layer consisting of 10 nm Titanium (for adhesion, not shown in the figure), 150 nm Cobalt, and 100 nm Aluminum, was sequentially deposited on the oxide disks using electron beam evaporation (SLOAN SL 1800) (Figure 2.30D). Finally, another 30 nm silicon dioxide

layer was deposited on the micromirrors by PECVD (STS Multiplex CVD) for bonding with PDMS.

PDMS substrates were prepared by spin coating uncured PDMS mixture (Sylgard 527: Sylgard 184 = 26:1) onto a glass slide and curing it on a hotplate at 60 °C for 48 hours. The rigid micromirrors on silicon and the PDMS substrate were exposed to oxygen plasma (500 mTorr, 80 Watts, 30 seconds, Technics RIE) before being mechanically bonded to each other (Figure 2.30E). The bonded structure was then placed into a beaker containing 55% acetone and 45% water and put into an ultrasonic water bath to break the silicon neck at the interface between the micromirrors and silicon anchors (Figure 2.30F). This process left the grating micromirrors (with metal) bonded on the PDMS substrate (Figure 2.30G).

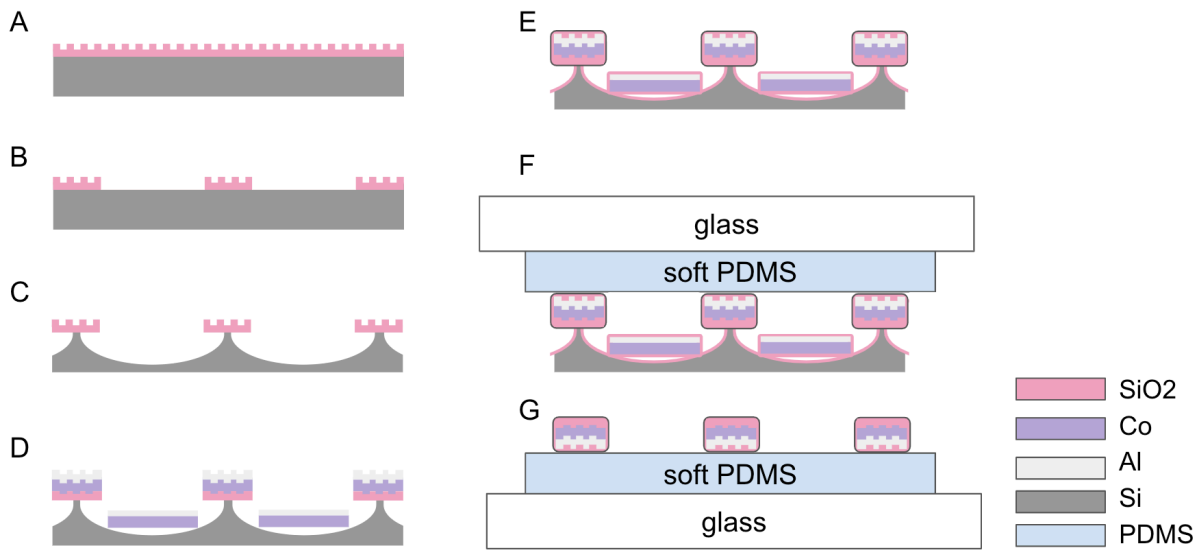

Figure 2.30. Fabrication of OMA device

(A) pattering grating structure by photoresist (SPR 700) with ASML Stepper, SiO_2 dry etch, and photoresist removal. (B) Micromirrors patterning with photoresist (KLT 5315) by Karl Suss MA6 and SiO_2 dry etch to form isolated micromirrors. (C) Si isotropic dry etch to undercut the substrate. (D) Metal electron beam deposition (Co/Al). (E) SiO2 coating with PECVD. (F) Oxygen plasma applied on both sides and bonding. (G) device released in acetone/water mixture solution.

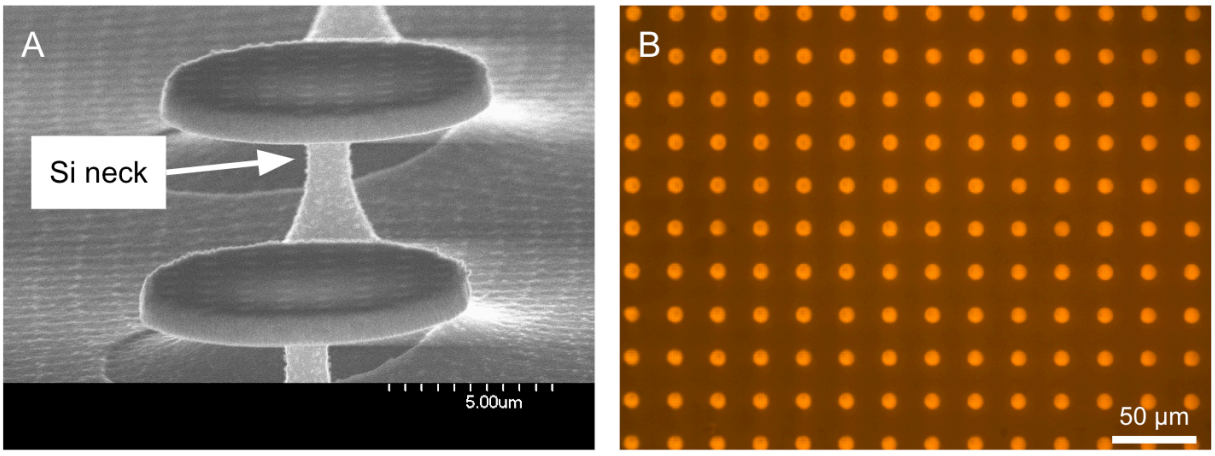

Figure 2.31. Images of Co micromirrors.

(A) SEM image or Co micromirrors on a Si wafer before bonded to PDMS substrate (Figure 2.30 D). (B) Microscope image of Co micromirrors bonded onto PDMS substrate at 40X magnification.

Chapter 3. Results and Discussion

To assess the capability of our OMA platform in measuring the stiffness of biomimetic materials, we conduct both experiments and simulation modeling. In the experiment, we attached soft PDMS samples with different stiffness levels to mimic a range of soft biological tissues at various locations on the device. By applying a magnetic field, we actuate the micromirror arrays and measure the changes of tilting angles at these regions.

In the simulation aspect, we construct a model that incorporates micromirror arrays embedded between a PDMS substrate and biomimetic materials of different stiffness. This model is also subjected to a magnetic field, with micromirror dimensions and material properties matching those in the experimental setup. Through this simulation, we generate a fitting curve that characterizes the relationship between material stiffness and tilting angle. This stiffness calibration curve is then compared with the experimental data to obtain the stiffness of materials. Figure 3.1 provides an overview of the process flow for measuring the stiffness of biomimetic materials. A more detailed description of the procedures is listed the subsequent sections.

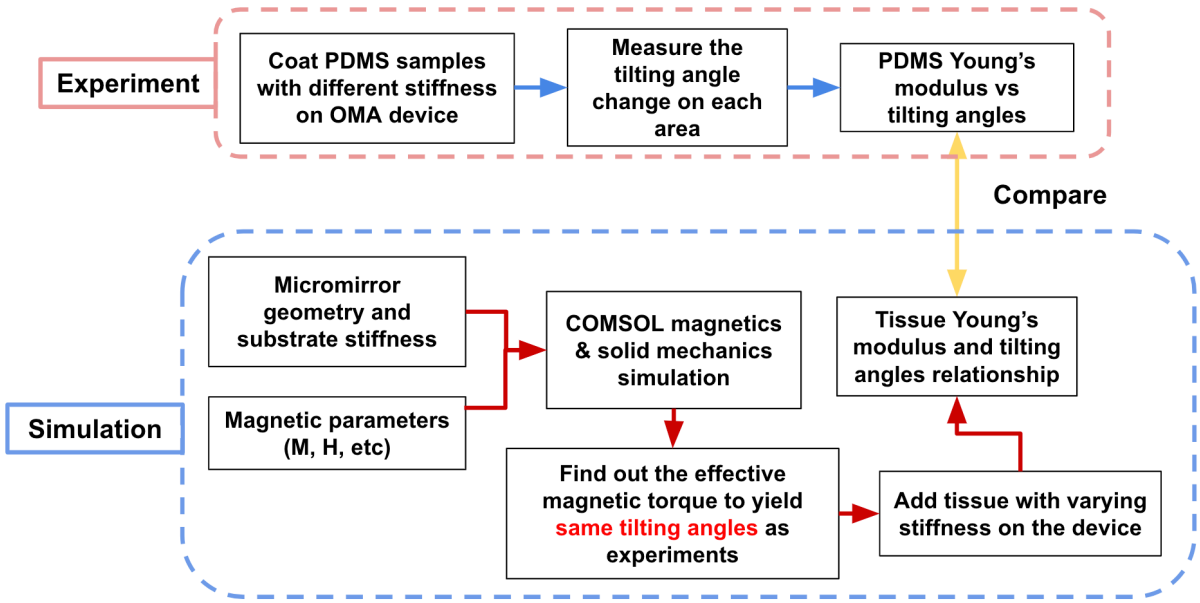

Figure 3.1. The method to build up correlation between biomimetic material stiffness and experimentally measured tilting angles.

3.1 Biomimetic material stiffness measurements

We first conducted an experimental analysis to characterize the stiffness of biomimetic materials on our OMA platforms. This involved the measurement of different PDMS samples with varying mixing ratios between Sylgard 527 and Sylgard 184, as outlined in Table 3.1 and Table 3.2. The purpose was to establish a correlation between material stiffness and the resulting micromirror tilting angle change on our OMA platform.

To mitigate the scattering effect caused by the significant refractive index difference at the edges of PDMS, we employed a black PDMS film created by incorporating carbon nanotubes (CNTs) into the PDMS mixture (Figure 3.2). The CNT-PDMS film fabrication is prepared by

mixing 1% wt of CNT into PDMS mixture (Sylgard 527:Sylgard 184 = 5:1) to form a sheet of around 500 µm and cure overnight at 60ºC.

Table 3.1. The PDMS mixing ratio and measured Young's modulus for Device A.

The Young's modulus of each sample is measured with nanoindentation

PDMS ratio	No PDMS	Sylgard 527 A:B = 1:1	Sylgard 527 A:B = 5:4	Sylgard 527:184 = 40:1	Sylgard 527:184 = 30:1	Sylgard 527:184 = 26:1	Sylgard 527:184 = 20:1	Sylgard 527:184 = 15:1	Sylgard 527:184 = 10:1	Sylgard 527:184 = 5:1
Measured Young's modulus (kpa)	N/A	8.48	13.74	29.80	33.59	43.146	49.54	57.45	70.31	177.99
Region in stiffness map	a	c	b	d	e	N/A	f	g	h	i

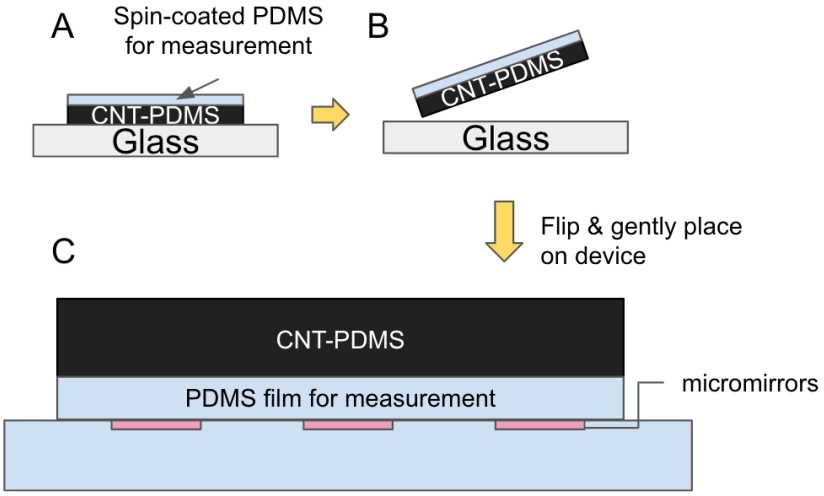

Figure 3.2. The process flow for preparing PDMS samples attached on an OMA device.

(A) Spin-coat the PDMS onto a small piece of the CNT-PDMS sheet. (B) Pick up and flip the composite sample. (C) Attach the sample onto OMA device and wait 24 hr for curing.

Subsequently, we spin-coat the PDMS (1000 rpm, 60 sec) to be measured (with a thickness > 30 µm) onto a small piece of the CNT-PDMS sheet, creating a composite sample. We flipped and placed the composite sample onto the micromirror platform before curing the

PDMS, ensuring minimal disruption to the micromirrors (Figure 3.2). This process was repeated for all PDMS samples, and PDMS thin films were allowed to cure naturally at room temperature for a duration of 24 hours. All the PDMS samples are prepared with 10% wt of PDMS platinum-based catalyst unless labeled with “no Pt” in the tables. To facilitate accurate measurements and prevent optical scattering, we enclosed the micromirrors area with a CNT-PDMS well, infused it with water, and capped it with another CNT-PDMS film that serves as a black background.

Figure 3.3A illustrates a stiffness map depicting the net tilting angle change across the entire field of view (5.1 mm × 7.2 mm) of an OMA device (Device A) during the stiffness measurement process. This map was generated by subtracting the tilting angle plot observed after magnetic actuation from the one obtained before magnetic actuation. The results clearly delineate distinct regions (a-i) with PDMS samples of different stiffness, each exhibiting different degrees of tilting angle change. To avoid edge effects, we carefully selected micromirrors located away from the PDMS edges and computed their average tilting angle change, serving as representative data for each sample for its Young's modulus calculation. Notably, the open area (region a, without any material attached) shows an average tilting angle of 3.66 degree, which will be used as a baseline tilting angle for simulation in the next section.

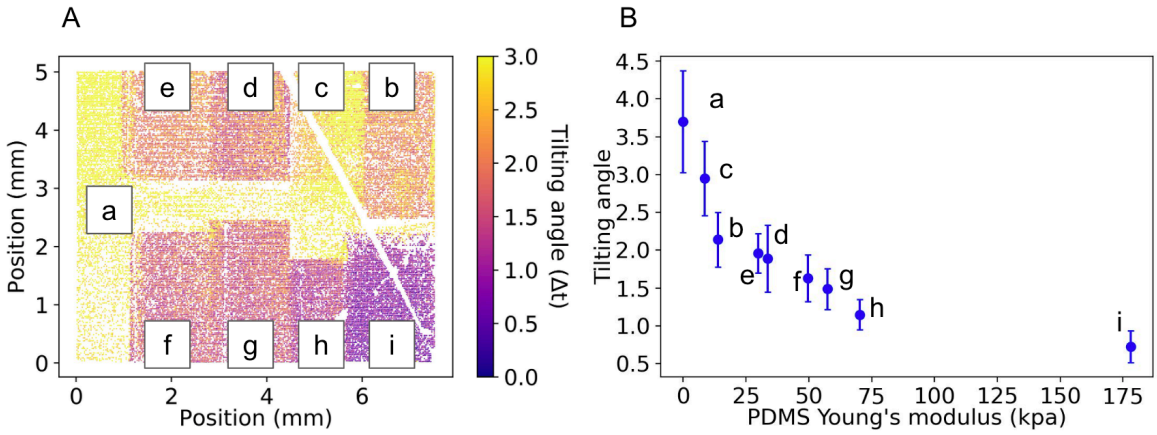

Figure 3.3. Stiffness measurement result of Device A.

(A) The tilting angle map. Each region is attached to PDMS with different stiffness and demonstrates different tilting angles. White areas depict missing or damaged micromirrors due to fabrication defect. Area a-i represent the tilting angle change in different regions covered with different PDMS stiffness (B) the correlation between tilting angle and PDMS Young's modulus.

In addition, to validate the Young's moduli of the PDMS samples attached on the OMA platform, we employed a widely-used instrumentation called nanoindentation for measuring PDMS samples. It is important to note that the measurements performed on the OMA platform involve thin film PDMS samples with a thickness ranging from 30 µm to 70 µm, which may yield different Young's modulus values compared to the bulk properties of PDMS [86]. To address this, during the preparation of each of the CNT-PDMS composite samples for OMA measurements, we also prepared an additional sample by spin-coating each PDMS sample onto glass substrates separately, using the same spin coating parameters, to enable separate thin-film measurements. The instrument we use is called nanoindenter (Pavone, Optics11 Life), which is a standard machine used for measuring thin film mechanical properties of biological materials. Table 3.1 presents the verified Young's moduli of each PDMS sample, along with their

corresponding mixing ratios. Subsequently, we incorporated the quantified Young's modulus data from the nanoindentation measurements into our measurement results obtained on the OMA platform to obtain the relationship between tilting angle change and PDMS samples' Young's modulus (Figure 3.3B).

Furthermore, we performed an additional stiffness measurement experiment using another device (Device B) that exhibited larger tilting angle responses. This difference in tilting angles could be attributed to a softer PDMS substrate. Figure 3.4A illustrates a stiffness map (regions a-e) with a field of view (FOV) of 5 mm x 5.5 mm, following the same concept as Figure 3.3A, but with a tilting angle of 5.1 degrees in the open region (region a). We repeat such measurements on different devices with same tilt response (not shown in Figure 3.4A) and collect the data points in Figure 3.4B to obtain the correlation between tilting angle and PDMS stiffness. The corresponding Young's modulus values for each PDMS sample are presented in Table 3.2 for reference.

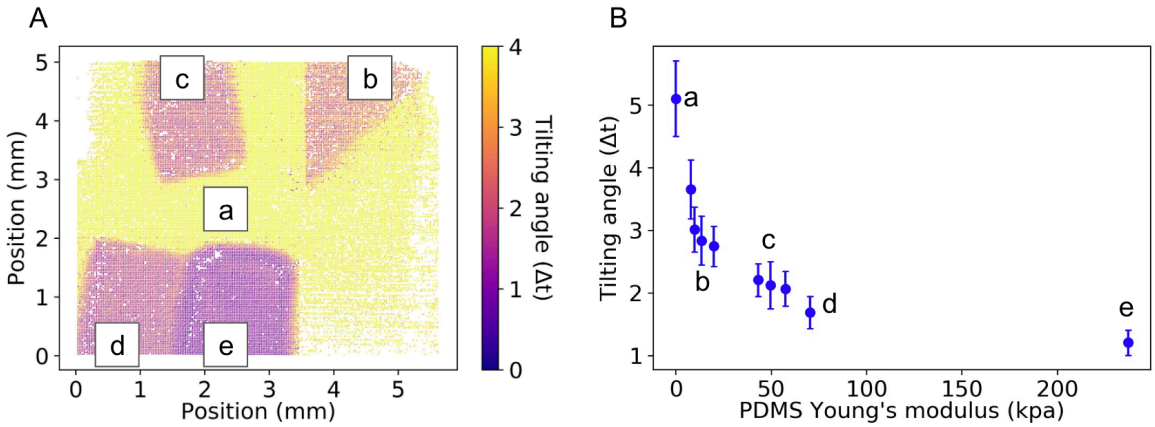

Figure 3.4. Stiffness measurement result of device B with larger tilt response.

(A) The tilting angle map. Each region is attached to PDMS with different stiffness. White areas depict missing or damaged micromirrors due to fabrication defect. (B) the correlation between tilting angle and PDMS Young's modulus (some datapoints are from other devices with the same tilt response).

Table 3.2. The PDMS mixing ratio and measured Young's modulus for device B and other devices.

PDMS ratio	No PDMS	Sylgard 527 A:B = 1:1 no Pt	Sylgard 527 A:B = 1:1 With Pt	Sylgard 527 A:B = 4:5	Sylgard 527 A:B = 2:3	Sylgard 527:184 = 50:1	Sylgard 527:184 = 20:1	Sylgard 527:184 = 15:1	Sylgard 527:184 = 10:1	Sylgard 527:184 = 5:1
Measured Young's modulus (kpa)	N/A	8.53	10.35	12.96	16.35	19.68	56.41	65.83	81.45	237.52
Region in stiffness map	a	N/A	b	N/A	N/A	N/A	c	N/A	d	e

3.2 COMSOL simulation

In COMSOL simulation we model biomimetic materials with varying Young's modulus to determine the relationship between the change of micromirror tilting angle and the material stiffness under magnetic field rotation. The simulation was performed by combining the Magnetics AC/DC module and Solid Mechanics module in COMSOL. Our model consists of 25

cobalt micromirrors sandwiched between a 10 µm biomimetic material layer and a 30 µm PDMS substrate, all placed within a fixed magnetic field (Figure 3.5A). The simulation generated a curve illustrating the relationship between the tissue's Young's modulus and the corresponding tilting angle change of the micromirrors.

In our experimental setup, we applied a magnetic field of 211 mT, which resulted in an average tilting angle of 3.6 degrees for Device A without anything on top of micromirrors, as determined through optical calibration data. Additionally, we measured the magnetization of our cobalt micromirrors under a sweep of applied fields using the SQUID magnetometer (MPMS3, Quantum Design Applications Inc.) to obtain the MH loop (Figure 3.5B).

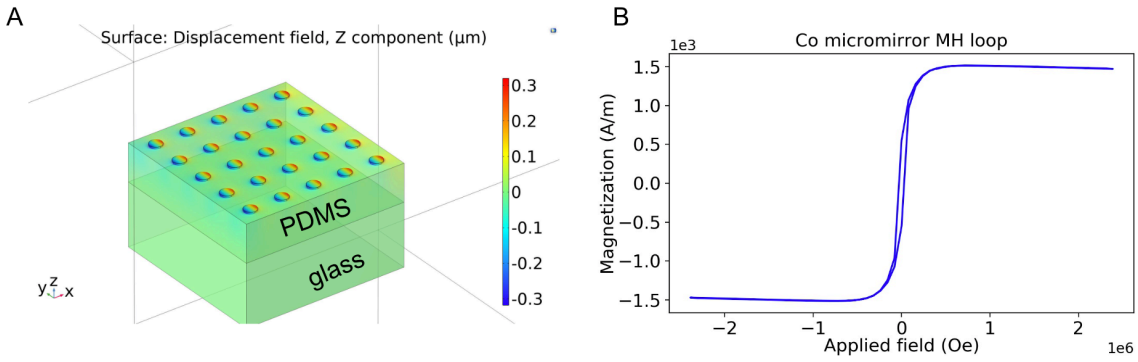

Figure 3.5. The simulation modeling and the applied magnetics parameters

(A) The simulated displacement of micromirrors in vertical (z) direction with an applied magnetic torque to match experiment result of 3.6 degree for Device A. (B) The measured MH loop of Co micromirrors, which is imported into simulation modeling to generate magnetic torque.

To ensure accuracy and account for material properties and experimental errors, we incorporated the measured magnetic parameters into the COMSOL simulation to determine the effective Young's modulus of the PDMS substrate in our device. This was done to achieve an equivalent tilting angle change of 3.6 degree for Device A without tissues on top of

micromirrors. The simulation yields an effective substrate Young's modulus of 15 kPa. However, we also performed stiffness measurements of the PDMS substrate (Sylgard 527:184 = 26:1) of our OMA devices using a nanoindenter, which yielded a value of 42 kPa. The significant disparity between the COMSOL-simulated effective modulus of 15 kPa and the directly measured value of 42 kPa would lead to substantial differences in the stiffness characterization curve due to the varying sensitivities of the different substrate stiffnesses.

Therefore, we decided to adjust the substrate's Young's modulus in COMSOL to 42 kPa to match with the measured value using the nanoindenter and subsequently modify the magnetic field value to achieve the resulting tilting angle of 3.6 degrees. This adjusted magnetic field value is referred to as our "effective magnetic field." By establishing this common baseline, we ensured consistency for comparison between the simulation and actual experimental results (Figure 3.5A).

Subsequently, we proceeded to incorporate a 10 μm biomimetic material layer onto the device and conducted a comprehensive analysis by sweeping through a range of Young's modulus values for the tissue. The parametric sweep encompassed values from 0 kPa to 200 kPa, with increments of 2.5 kPa. Through this process, we collected the corresponding tilting angles associated with each Young's modulus setting. These datasets were then exported from COMSOL for further analysis.

Utilizing the exported datasets, we plotted a curve illustrating the relationship between tissue Young's modulus and the resulting tilting angle change (Figure 3.6A). To establish a functional relationship, we employed a curve fitting model (PyEarth) in Python to fit the data. The outcome of this analysis indicated an exponential-like correlation between tissue Young's modulus and the micromirror tilting angle change.

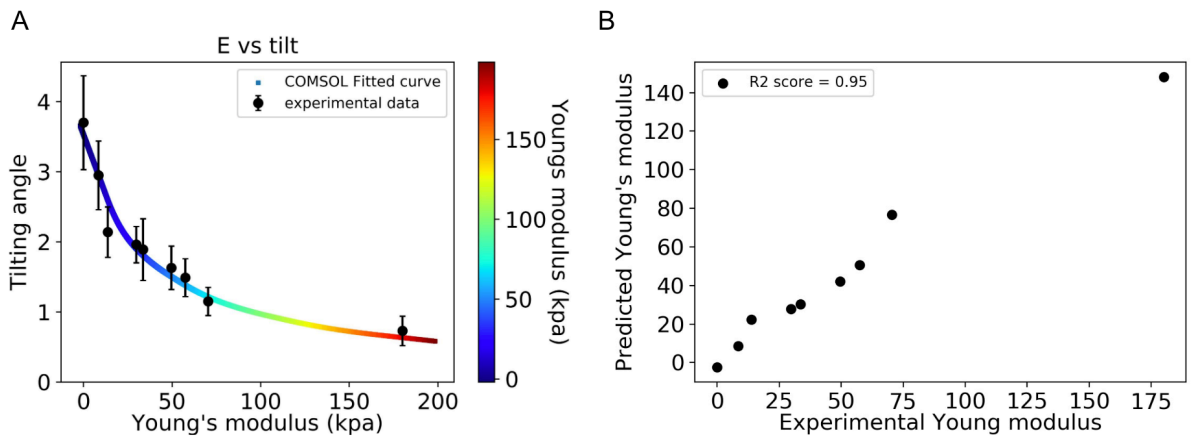

Figure 3.6. The correlation between micromirrors tilting angles and PDMS Young's modulus.

(A) the fitting curve generated from simulation and data points from experiments show high agreement. (B) the relationship between experimental measured PDMS Young's modulus and predicted Young's modulus from COMSOL-generated curve shows a R2 score 0.95.

By incorporating the experimentally measured data points from Section 3.1 into the COMSOL curve, as depicted in Figure 3.6A, we observed a close agreement between the experimental data and the simulated curve. This finding indicates that the curve derived from the tilting angle measurements can serve as a reliable calibration curve for quantifying the stiffness of biomimetic materials within the range of 0-200 kPa. This suggests that the platform holds significant potential for characterizing biological tissue samples within this stiffness range. Notably, the curve exhibits more pronounced tilting angle changes within the Young's modulus range of 0-50 kPa, which aligns with the stiffness range commonly observed in biological tissues.

To validate the predictive accuracy of our platform, we plot the correlation between the experimental and predicted values in Figure 3.6B and calculate the coefficient of determination (R2 score). R2 score represents the proportion of variation in the dependent variable that can be

predicted from the independent variable(s). We obtained a R2 score of 0.95, indicating a good correlation between the experimental and predicted values.

Additionally, we applied the same steps as described above to the second device (Device B), which exhibited a larger tilting angle response (5.1º). To establish a common baseline between the simulation and experiments, we adjusted the magnetic torque in the COMSOL model to yield a tilting angle of 5.1 degrees, matching the experimental data. Figure 3.7A illustrates the tilt-Young's modulus correlation generated from the modified COMSOL model for the second device. We also incorporated the experimental data from the second device into this curve for comparison, which led us to reach the same conclusion. Figure 3.7B shows the correlation between experimentally measured Young's modulus and predicted values. These results highlight the platform's sensitivity in detecting soft biological tissues and its potential for numerous biomedical applications, including disease diagnosis and cancer research.

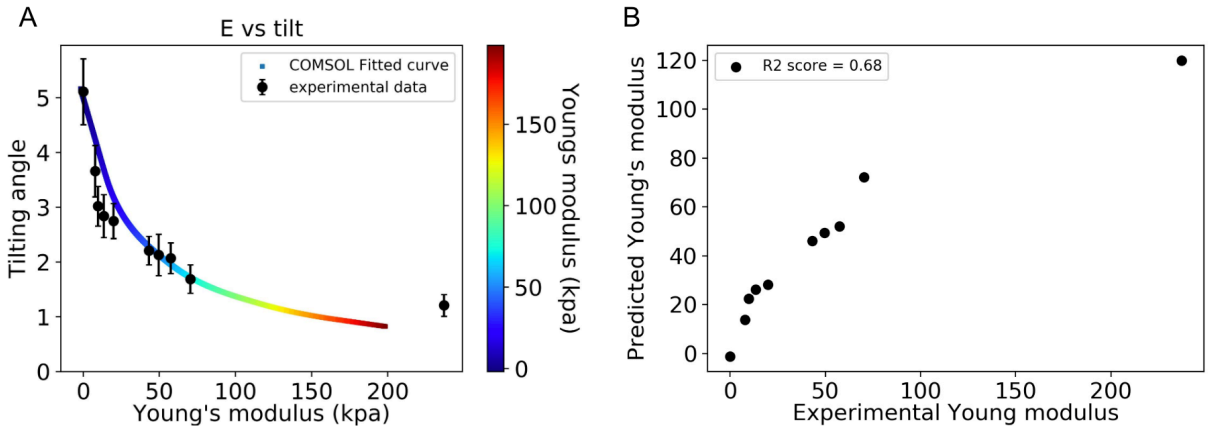

Figure 3.7. The correlation between micromirrors tilting angles and PDMS Young's modulus of Device B. (A) the fitting curve generated from simulation and data points from experiments. (B) the relationship between experimental measured PDMS Young's modulus and predicted Young's modulus from COMSOL-generated curve shows a R2 score 0.68.

3.3 Re-validate the Young's modulus of biomimetic materials

Given that the current data acquired from OMA pertains to the alteration of tilting angles, we have devised a validation approach to assess OMA's efficacy in quantifying the Young's modulus of biomimetic tissues. This approach involves employing the measured tilting angle data (as discussed in Section 3.1) and inputting it into the stiffness calibration curve (detailed in Section 3.2). By doing so, we predict the PDMS stiffness within each area, subsequently comparing the predicted Young's modulus from OMA with the validated Young's modulus derived from the nanoindenter measurements. The predicted Young's modulus maps for Device A and Device B are presented in Figure 3.8A and Figure 3.9A, respectively. A comparison between these two results is also presented in Figure 3.8B and Figure 3.9B respectively, where each column in the bar charts represents the average value of each PDMS region.

In particular, the OMA device notably exhibits high sensitivity in regions b-e, as depicted in Figure 3.8A, where PDMS stiffness levels are comparatively softer. The anticipated Young's modulus values obtained from OMA for these regions are 8.47 kPa, 22.41 kPa, 27.75 kPa, and 30.26 kPa, respectively. Correspondingly, the results yielded by nanoindentation measurements are 8.48 kPa, 13.74 kPa, 29.80 kPa, and 33.60 kPa. This comparison underscores a sensitivity of 5 kPa achieved by OMA in distinguishing stiffness difference within the Young's modulus range below 40 kPa, a realm wherein most single cells reside. In addition, it should be noted that the clear boundaries of each PDMS area (inset, Figure 3.8A and Figure 3.9A) demonstrate the spatial resolution achieved by the OMA device, which is equivalent to the micromirror period (26 μm). This level of resolution corresponds to single-cellular resolution as individual cells ranges between 30-50 μm, indicating the potential of our OMA device to quantify the stiffness of

biological tissues at the single-cellular level while maintaining the ability to measure collective cell sheets and larger tissue-scale areas.

On the other hand, we observed a discrepancy between the results predicted by the OMA platform and those measured by nanoindentation in Figure 3.8B and Figure 3.9B, particularly in the softer and stiffer ranges. Notably, the OMA-predicted values were higher than the nanoindenter-measured values in the softer range, while the opposite trend was observed in the stiffer range. This discrepancy can be attributed to the tilting angles measured by the OMA platform (Figure 3.6A and 3.7A), which were larger than the tilting angles captured in the stiffness calibration curve in the stiffer range, and smaller than those in the softer range. These differences in tilting angles contribute to the differences observed between the OMA-predicted and nanoindenter-measured results.

The error bars in the OMA's results represent the standard deviation of the predicted values obtained from each area. The predicted stiffness heterogeneity exist within each PDMS area may imply the local stiffness difference or distribution due to the cross-linking inside PDMS material. Huang et al. [87] conducted a study using AFM to map PDMS stiffness within a 1 μm × 1 μm area, revealing heterogeneous stiffness distribution. This indicates that stiffness nonuniformity can exist within PDMS, even when the mixing ratio is controlled. In our measurement approach, each PDMS-covered area on the OMA device is larger, spanning more than 1 mm × 2 mm and encompassing several hundred micromirror data points. In contrast, the nanoindentation measurement only captures approximately 5 data points per sample, which may not be fully representative of the stiffness variations within each PDMS area.

In mechanobiology studies, it's recognized that most cancer cells are at least 50% softer than their non-cancerous counterparts [36]. While the observed standard deviation in the

predicted Young's modulus introduces around a 30% variation around the average value, our findings continue to suggest the potential to distinguish cancer cells from normal cells, even within a tissue-level field of view.

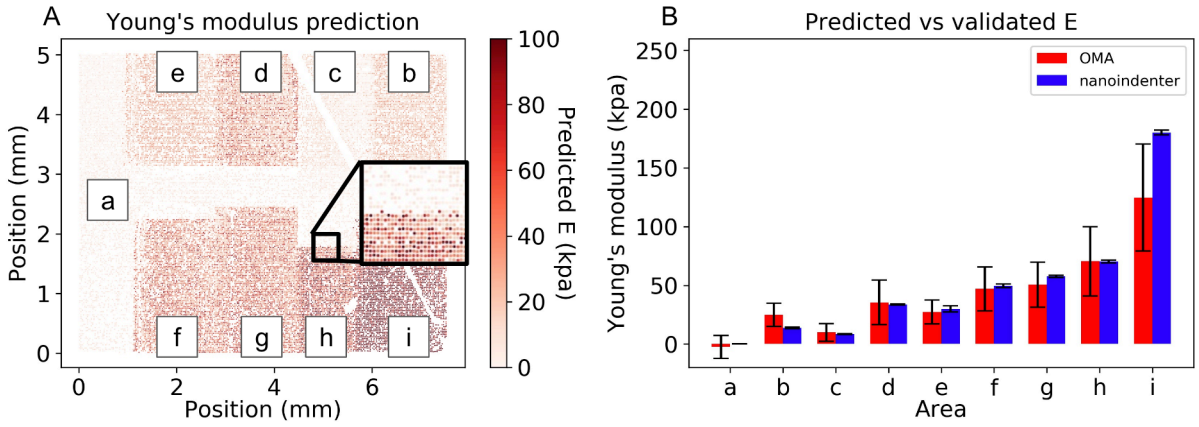

Figure 3.8. The PDMS stiffness predcition of Device A.

(A) The predcited stiffness map. The clear boundaries of each area demonstrate a micron-scale spatial resolution. (B) The comparison between OMA's predicted Young's modulus and the validated Young's modulus with the nanoindenter.

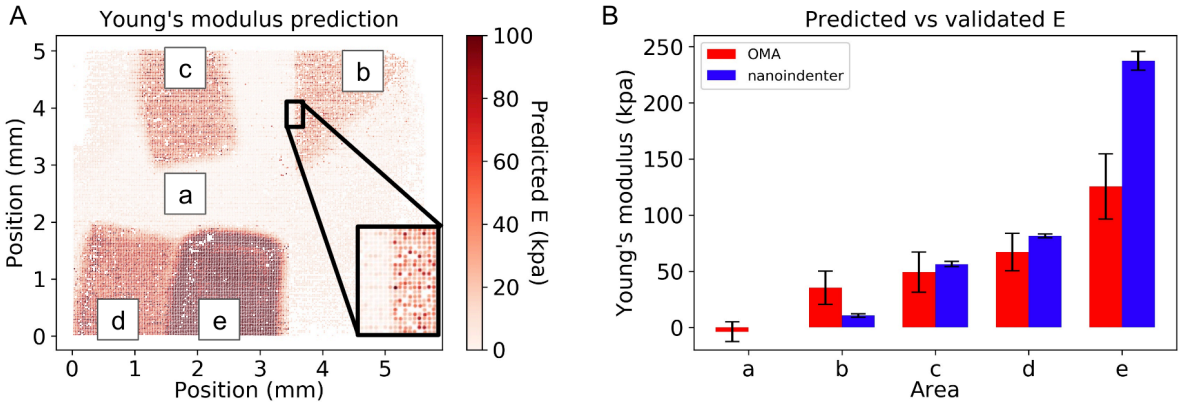

Figure 3.9. The PDMS stiffness re-validation of Device B.

(A) The predicted stiffness map. The clear boundaries of each area (inset) demonstrate a micron-scale spatial resolution. (B) The comparison between OMA's predicted Young's modulus and the validated Young's modulus with the nanoindenter.

Chapter 4. Conclusion

The cellular elastic modulus has emerged as a valuable indicator for differentiating cellular states. However, existing techniques for measuring cellular stiffness are limited in their ability to assess only a small number of cells at a time, preventing the concurrent evaluation of multi-cellular systems. This limitation hampers the investigation of collective cell behaviors and dynamic tissue structure changes during disease progression.

The Optomagnetic Micromirror Arrays (OMA) platform addresses these limitations by employing over 50,000 magnetic micromirrors with sub-micron grating structures embedded in a PDMS substrate. With a field of view of 5.1 mm × 7.2 mm, the OMA platform promises tissue-level and the scale of collective cells measurements. Each individual micromirror can be magnetically actuated, allowing for the probing of local stiffness of biomimetic material at a single-cell spatial resolution, rather than assessing bulk properties. The calibrated OMA platform is capable of quantifying the elastic modulus of biomimetic materials within the range of 0-200 kPa, which encompasses the stiffness range commonly observed in biological tissues and cells. In addition, the white light illumination and image sensor's capability to collect optical signals from underneath the device also help avoid potential issues caused by biological sample opacity, as discussed in Section 3.3. Consequently, this platform promises for tissue-level assessments while preserving the single-cellular resolution of stiffness mapping.

There are several aspects that can be improved in the OMA platform, particularly in terms of fabrication and optical setup design. In the fabrication aspect, one limitation of the current OMA device when measuring real biological samples is the oxidation of the magnetic material in the biological environment during cell culturing period in an incubator. The elevated

temperature and humidity can penetrate the thin oxide protection layer of the Co micromirrors, causing oxidation of the Co and rendering it unable to be magnetically actuated. Therefore, it is necessary to incorporate a more sustainable passivation layer to protect the micromirrors. An ideal candidate for this purpose is aluminum oxide, a material widely used in the semiconductor industry as a metal passivation layer. By applying Atomic Layer Deposition (ALD), an additional Al_2O_3 thin layer can be deposited onto the Co micromirrors (Figure 2.30D) before coating them with SiO_2. This will enable the OMA device for probing the stiffness of real biological samples.

Additionally, the current Young's modulus of the PDMS substrate is relatively high at 42 kPa compared to most biological tissues. Consequently, when measuring biological samples with an elastic modulus lower than 42 kPa, the contribution of stiffness to the micromirror tilting angle change becomes smaller compared to that of the substrate. Therefore, fabricating a softer substrate is crucial to enhance the sensitivity of the OMA platform.

To further improve the spatial resolution of the OMA platform, the pitch of the micromirrors can be reduced. The current pitch of 26 μm has already demonstrated negligible optical and mechanical coupling (<1%), indicating that a smaller pitch is possible for enhancing the spatial resolution while maintaining tolerable coupling between adjacent micromirrors.

The current setups suffer from bulkiness and limited space due to the presence of large LED and fan sets. These limitations hinder the rotation of the magnets up to 30º. However, by changing the direction of illumination from its current configuration to a vertical illumination angle towards the device, we can reposition the camera to detect the 2nd order diffraction. This adjustment will significantly enhance the rotation capability of the magnets and provide greater flexibility in designing the magnetic setup.

Reference

1. Suresh, S. (2007). Biomechanics and biophysics of cancer cells. *Acta biomaterialia* , *3*(4), 413-438.
2. Darling, E. M., & Di Carlo, D. (2015). High-throughput assessment of cellular mechanical properties. *Annual review of biomedical engineering*, *17*, 35-62.
3. Moeendarbary, E., & Harris, A. R. (2014). Cell mechanics: principles, practices, and prospects. *Wiley Interdisciplinary Reviews: Systems Biology and Medicine*, *6*(5), 371-388.
4. Khatau, S. B., Bloom, R. J., Bajpai, S., Razafsky, D., Zang, S., Giri, A., ... & Wirtz, D. (2012). The distinct roles of the nucleus and nucleus-cytoskeleton connections in three-dimensional cell migration. *Scientific reports*, *2*(1), 1-11.
5. Roca-Cusachs, P., Alcaraz, J., Sunyer, R., Samitier, J., Farré, R., & Navajas, D. (2008). Micropatterning of single endothelial cell shape reveals a tight coupling between nuclear volume in G1 and proliferation. *Biophysical journal* , *94*(12), 4984-4995.
6. Zwerger, M., Ho, C. Y., & Lammerding, J. (2011). Nuclear mechanics in disease. *Annual review of biomedical engineering*, *13*, 397-428.
7. Luo, Q., Kuang, D., Zhang, B., & Song, G. (2016). Cell stiffness determined by atomic force microscopy and its correlation with cell motility. *Biochimica et Biophysica Acta (BBA)-General Subjects*, *1860* (9), 1953-1960.
8. Blanchoin, L., Boujemaa-Paterski, R., Sykes, C., & Plastino, J. (2014). Actin dynamics, architecture, and mechanics in cell motility. *Physiological reviews* , *94*(1), 235-263.

9. Gruenbaum, Y., & Aebi, U. (2014). Intermediate filaments: a dynamic network that controls cell mechanics. *F1000prime reports*, *6*.
10. Qin, Z., Kreplak, L., & Buehler, M. J. (2009). Hierarchical structure controls nanomechanical properties of vimentin intermediate filaments. *PloS one*, *4*(10), e7294.
11. Rathje, L. S. Z., Nordgren, N., Pettersson, T., Rönnlund, D., Widengren, J., Aspenström, P., & Gad, A. K. (2014). Oncogenes induce a vimentin filament collapse mediated by HDAC6 that is linked to cell stiffness. *Proceedings of the National Academy of Sciences* , *111* (4), 1515-1520.
12. Fletcher, D. A., & Mullins, R. D. (2010). Cell mechanics and the cytoskeleton. *Nature* , *463* (7280), 485-492.
13. Ouyang, H., Nauman, E., & Shi, R. (2013). Contribution of cytoskeletal elements to the axonal mechanical properties. *Journal of biological engineering*, *7*(1), 1-8.
14. Kumar, Y., & Valdivia, R. H. (2008). Reorganization of the host cytoskeleton by the intracellular pathogen Chlamydia trachomatis. *Communicative & integrative biology* , *1*(2), 175-177.
15. Dulińska, I., Targosz, M., Strojny, W., Lekka, M., Czuba, P., Balwierz, W., & Szymoński, M. (2006). Stiffness of normal and pathological erythrocytes studied by means of atomic force microscopy. *Journal of biochemical and biophysical methods* , *66*(1-3), 1-11.
16. Suresh, S. (2007). Elastic clues in cancer detection. *Nature Nanotechnology* , *2*(12), 748-749.

17. Ferrari, S., & Pesce, M. (2021). Stiffness and aging in cardiovascular diseases: the dangerous relationship between force and senescence. *International Journal of Molecular Sciences* , *22*(7), 3404.
18. Wang, L., Xia, J., Li, J., Hagemann, T. L., Jones, J. R., Fraenkel, E., ... & Feany, M. B. (2018). Tissue and cellular rigidity and mechanosensitive signaling activation in Alexander disease. *Nature communications*, *9*(1), 1899.
19. Suresh, S. (2007). Biomechanics and biophysics of cancer cells. *Acta biomaterialia* , *3*(4), 413-438.
20. Kumar, S., & Weaver, V. M. (2009). Mechanics, malignancy, and metastasis: the force journey of a tumor cell. *Cancer and Metastasis Reviews*, *28*, 113-127.
21. Swaminathan, V., Mythreye, K., O'Brien, E. T., Berchuck, A., Blobe, G. C., & Superfine, R. (2011). Mechanical stiffness grades metastatic potential in patient tumor cells and in cancer cell lines mechanical stiffness of cells dictates cancer cell invasion. *Cancer research*, *71*(15), 5075-5080.
22. Ong, M. S., Deng, S., Halim, C. E., Cai, W., Tan, T. Z., Huang, R. Y. J., ... & Yap, C. T. (2020). Cytoskeletal proteins in cancer and intracellular stress: a therapeutic perspective. *Cancers* , *12*(1), 238.
23. Paszek, M. J., Zahir, N., Johnson, K. R., Lakins, J. N., Rozenberg, G. I., Gefen, A., ... & Weaver, V. M. (2005). Tensional homeostasis and the malignant phenotype. *Cancer cell*, *8*(3), 241-254.
24. Wullkopf, L., West, A. K. V., Leijnse, N., Cox, T. R., Madsen, C. D., Oddershede, L. B., & Erler, J. T. (2018). Cancer cells' ability to mechanically adjust to extracellular matrix

stiffness correlates with their invasive potential. *Molecular biology of the cell*, *29* (20), 2378-2385.

25. Pawlak, G., & Helfman, D. M. (2001). Cytoskeletal changes in cell transformation and tumorigenesis. *Current opinion in genetics & development*, *11*(1), 41-47.
26. Xu, W., Mezencev, R., Kim, B., Wang, L., McDonald, J., & Sulchek, T. (2012). Cell stiffness is a biomarker of the metastatic potential of ovarian cancer cells.
27. Liu, H., Tan, Q., Geddie, W. R., Jewett, M. A., Phillips, N., Ke, D., ... & Sun, Y. (2014). Biophysical characterization of bladder cancer cells with different metastatic potential. *Cell biochemistry and biophysics*, *68*, 241-246.
28. Watanabe, T., Kuramochi, H., Takahashi, A., Imai, K., Katsuta, N., Nakayama, T., ... & Suganuma, M. (2012). Higher cell stiffness indicating lower metastatic potential in B16 melanoma cell variants and in (−)-epigallocatechin gallate-treated cells. *Journal of cancer research and clinical oncology*, *138*, 859-866.
29. Heath, J. R., Ribas, A., & Mischel, P. S. (2016). Single-cell analysis tools for drug discovery and development. *Nature reviews Drug discovery*, *15*(3), 204-216.
30. Hodzic, E. (2016). Single-cell analysis: Advances and future perspectives. *Bosnian journal of basic medical sciences*, *16*(4), 313.
31. Krieg, M., Fläschner, G., Alsteens, D., Gaub, B. M., Roos, W. H., Wuite, G. J., ... & Müller, D. J. (2019). Atomic force microscopy-based mechanobiology. *Nature Reviews Physics*, *1*(1), 41-57.
32. Rotsch, C., & Radmacher, M. (2000). Drug-induced changes of cytoskeletal structure and mechanics in fibroblasts: an atomic force microscopy study. *Biophysical journal*, *78*(1), 520-535.

33. Hao, Y., Cheng, S., Tanaka, Y., Hosokawa, Y., Yalikun, Y., & Li, M. (2020). Mechanical properties of single cells: Measurement methods and applications. *Biotechnology Advances*, *45*, 107648.

34. Hertz, H. (1882). Ueber die Berührung fester elastischer Körper.

35. Sneddon, I. N. (1965). The relation between load and penetration in the axisymmetric Boussinesq problem for a punch of arbitrary profile. *International journal of engineering science*, *3*(1), 47-57.

36. Lekka, M. (2016). Discrimination between normal and cancerous cells using AFM. *Bionanoscience*, *6*, 65-80.

37. Liu, H., Tan, Q., Geddie, W. R., Jewett, M. A., Phillips, N., Ke, D., ... & Sun, Y. (2014). Biophysical characterization of bladder cancer cells with different metastatic potential. *Cell biochemistry and biophysics*, *68*, 241-246.

38. Xu, W., Mezencev, R., Kim, B., Wang, L., McDonald, J., & Sulchek, T. (2012). Cell stiffness is a biomarker of the metastatic potential of ovarian cancer cells.

39. Dulińska, I., Targosz, M., Strojny, W., Lekka, M., Czuba, P., Balwierz, W., & Szymoński, M. (2006). Stiffness of normal and pathological erythrocytes studied by means of atomic force microscopy. *Journal of biochemical and biophysical methods*, *66*(1-3), 1-11.

40. Hochmuth, R. M. (2000). Micropipette aspiration of living cells. *Journal of biomechanics*, *33*(1), 15-22.

41. Rand, R. P., & Burton, A. C. (1964). Mechanical properties of the red cell membrane: I. Membrane stiffness and intracellular pressure. *Biophysical journal*, *4*(2), 115-135.

42. Shojaei-Baghini, E., Zheng, Y., Jewett, M. A., Geddie, W. B., & Sun, Y. (2013). Mechanical characterization of benign and malignant urothelial cells from voided urine. *Applied Physics Letters*, *102*(12), 123704

43. Rowat, A. C., Lammerding, J., & Ipsen, J. H. (2006). Mechanical properties of the cell nucleus and the effect of emerin deficiency. *Biophysical journal*, *91*(12), 4649-4664.

44. Bustamante, C. J., Chemla, Y. R., Liu, S., & Wang, M. D. (2021). Optical tweezers in single-molecule biophysics. *Nature Reviews Methods Primers*, *1*(1), 25.

45. Zhang, H., & Liu, K. K. (2008). Optical tweezers for single cells. *Journal of the Royal Society interface*, *5*(24), 671-690.

46. Berg-Sørensen, K., & Flyvbjerg, H. (2004). Power spectrum analysis for optical tweezers. *Review of Scientific Instruments*, *75*(3), 594-612.

47. Neuman, K. C., & Block, S. M. (2004). Optical trapping. *Review of scientific instruments*, *75*(9), 2787-2809.

48. Suresh, S., Spatz, J., Mills, J. P., Micoulet, A., Dao, M., Lim, C. T., ... & Seufferlein, T. (2005). Connections between single-cell biomechanics and human disease states: gastrointestinal cancer and malaria. *Acta biomaterialia*, *1*(1), 15-30.

49. Guck, J., Schinkinger, S., Lincoln, B., Wottawah, F., Ebert, S., Romeyke, M., ... & Bilby, C. (2005). Optical deformability as an inherent cell marker for testing malignant transformation and metastatic competence. *Biophysical journal*, *88*(5), 3689-3698.

50. Buican, T. N., Smyth, M. J., Crissman, H. A., Salzman, G. C., Stewart, C. C., & Martin, J. C. (1987). Automated single-cell manipulation and sorting by light trapping. *Applied optics*, *26*(24), 5311-5316.

51. Chan, C. J., Whyte, G., Boyde, L., Salbreux, G., & Guck, J. (2014). Impact of heating on passive and active biomechanics of suspended cells. *Interface focus*, *4*(2), 20130069.

52. Huang, H., Kamm, R. D., & Lee, R. T. (2004). Cell mechanics and mechanotransduction: pathways, probes, and physiology. American Journal of Physiology-Cell Physiology, 287(1), C1-C11.

53. Hao, Y., Cheng, S., Tanaka, Y., Hosokawa, Y., Yalikun, Y., & Li, M. (2020). Mechanical properties of single cells: Measurement methods and applications. Biotechnology Advances, 45, 107648.

54. Swaminathan, V., Mythreye, K., O'Brien, E. T., Berchuck, A., Blobe, G. C., & Superfine, R. (2011). Mechanical stiffness grades metastatic potential in patient tumor cells and in cancer cell lines. Cancer research, 71(15), 5075-5080.

55. Rørth P (2009) Collective cell migration. Annu Rev Cell Dev Biol 25:407–429]

56. Weijer CJ (2009) Collective cell migration in development. J Cell Sci122: 3215–3223

57. Barriga, E. H., Franze, K., Charras, G., & Mayor, R. (2018). Tissue stiffening coordinates morphogenesis by triggering collective cell migration in vivo. *Nature*, *554*(7693), 523-527.

58. Friedl P, Gilmour D (2009) Collective cell migration in morphogenesis, regeneration and cancer. Nat Rev Mol Cell Biol 10: 445–457

59. Friedl P, Locker J, Sahai E, Segall JE (2012) Classifying collective cancer cell invasion. Nat Cell Biol 14: 777–783

60. De Pascalis, C., & Etienne-Manneville, S. (2017). Single and collective cell migration: the mechanics of adhesions. Molecular biology of the cell, 28(14), 1833-1846.

61. Rørth, P. (2012). Fellow travellers: emergent properties of collective cell migration. EMBO reports, 13(11), 984-991.

62. Yamamoto, E., Kohama, G., Sunakawa, H., Iwai, M. & Hiratsuka, H. Mode of invasion, bleomycin sensitivity, and clinical course in squamous cell carcinoma of the oral cavity. Cancer 51, 2175–2180 (1983)

63. DiCostanzo, D., Rosen, P. P., Gareen, I., Franklin, S. & Lesser, M. Prognosis in infiltrating lobular carcinoma. An analysis of 'classical' and variant tumors. Am. J. Surg. Pathol. 14, 12–23 (1990).

64. Chen, B. J., Wu, J. S., Tang, Y. J., Tang, Y. L. &Liang, X. H. What makes leader cells arise: intrinsic properties and support from neighboring cells. J. Cell. Physiol. 235, 8983–8995 (2020).

65. Swaminathan, V., Mythreye, K., O'Brien, E. T., Berchuck, A., Blobe, G. C., & Superfine, R. (2011). Mechanical stiffness grades metastatic potential in patient tumor cells and in cancer cell linesmechanical stiffness of cells dictates cancer cell invasion. Cancer research , 71 (15), 5075-5080.

66. Raudenska, M., Kratochvilova, M., Vicar, T., Gumulec, J., Balvan, J., Polanska, H., ... & Masarik, M. (2019). Cisplatin enhances cell stiffness and decreases invasiveness rate in prostate cancer cells by actin accumulation. Scientific reports, 9(1), 1660.

67. Handorf, A. M., Zhou, Y., Halanski, M. A., & Li, W. J. (2015). Tissue stiffness dictates development, homeostasis, and disease progression. *Organogenesis*, *11*(1), 1-15.

68. Kass, L., Erler, J. T., Dembo, M., & Weaver, V. M. (2007). Mammary epithelial cell: influence of extracellular matrix composition and organization during development and

tumorigenesis. *The international journal of biochemistry & cell biology*, *39*(11), 1987-1994.

69. Butcher, D. T., Alliston, T., & Weaver, V. M. (2009). A tense situation: forcing tumour progression. *Nature Reviews Cancer*, *9*(2), 108-122.
70. Paszek, M. J., Zahir, N., Johnson, K. R., Lakins, J. N., Rozenberg, G. I., Gefen, A., ... & Weaver, V. M. (2005). Tensional homeostasis and the malignant phenotype. *Cancer cell*, *8*(3), 241-254.
71. Handorf, A. M., Zhou, Y., Halanski, M. A., & Li, W. J. (2015). Tissue stiffness dictates development, homeostasis, and disease progression. *Organogenesis*, *11*(1), 1-15.
72. Krouskop, T. A., Wheeler, T. M., Kallel, F., Garra, B. S., & Hall, T. (1998). Elastic moduli of breast and prostate tissues under compression. *Ultrasonic imaging*, *20*(4), 260-274.
73. Mierke, C. T. (2019). The matrix environmental and cell mechanical properties regulate cell migration and contribute to the invasive phenotype of cancer cells. *Reports on Progress in Physics*, *82*(6), 064602.
74. Plodinec, M., Loparic, M., Monnier, C. A., Obermann, E. C., Zanetti-Dallenbach, R., Oertle, P., ... & Schoenenberger, C. A. (2012). The nanomechanical signature of breast cancer. *Nature nanotechnology*, *7*(11), 757-765.
75. Lekka, M., Gil, D., Pogoda, K., Dulińska-Litewka, J., Jach, R., Gostek, J., ... & Laidler, P. (2012). Cancer cell detection in tissue sections using AFM. *Archives of biochemistry and biophysics*, *518*(2), 151-156.
76. Zhou, Z., Zheng, C., Li, S., Zhou, X., Liu, Z., He, Q., ... & Wang, A. (2013). AFM nanoindentation detection of the elastic modulus of tongue squamous carcinoma cells

with different metastatic potentials. *Nanomedicine: Nanotechnology, Biology and Medicine*, *9*(7), 864-874.

77. Cooney, G. M., Moerman, K. M., Takaza, M., Winter, D. C., & Simms, C. K. (2015). Uniaxial and biaxial mechanical properties of porcine linea alba. *Journal of the mechanical behavior of biomedical materials*, *41*, 68-82.

78. Griffin, M., Premakumar, Y., Seifalian, A., Butler, P. E., & Szarko, M. (2016). Biomechanical characterization of human soft tissues using indentation and tensile testing. *JoVE (Journal of Visualized Experiments)*, (118), e54872.

79. Hajjarian, Z., & Nadkarni, S. K. (2011, August). Measurement of bulk mechanical properties of tissue using laser speckle rheology. In *2011 Annual International Conference of the IEEE Engineering in Medicine and Biology Society* (pp. 5746-5748). IEEE.

80. Jorba, I., Uriarte, J. J., Campillo, N., Farré, R., & Navajas, D. (2017). Probing micromechanical properties of the extracellular matrix of soft tissues by atomic force microscopy. *Journal of cellular physiology*, *232*(1), 19-26.

81. Ozawa, H., Matsumoto, T., Ohashi, T., Sato, M., & Kokubun, S. (2001). Comparison of spinal cord gray matter and white matter softness: measurement by pipette aspiration method. *Journal of Neurosurgery: Spine*, *95*(2), 221-224.

82. Dos Santos, A. X. D. S., & Liberali, P. (2019). From single cells to tissue self-organization. *The FEBS Journal*, *286*(8), 1495.

83. Guimarães, C. F., Gasperini, L., Marques, A. P., & Reis, R. L. (2020). The stiffness of living tissues and its implications for tissue engineering. *Nature Reviews Materials*, 5(5), 351-370.

84. Judy, J. W. (1996). Batch-fabricated ferromagnetic microactuators with silicon flexures. University of California, Berkeley.

85. Grass, R. N., & Stark, W. J. (2006). Gas phase synthesis of fcc-cobalt nanoparticles. *Journal of Materials Chemistry*, *16*(19), 1825-1830.

86. Liu, M., Sun, J., Sun, Y., Bock, C., & Chen, Q. (2009). Thickness-dependent mechanical properties of polydimethylsiloxane membranes. *Journal of micromechanics and microengineering, 19*(3), 035028.

87. Huang, H., Dobryden, I., Thorén, P. A., Ejenstam, L., Pan, J., Fielden, M. L., ... & Claesson, P. M. (2017). Local surface mechanical properties of PDMS-silica nanocomposite probed with Intermodulation AFM. *Composites Science and Technology, 150*, 111-119.